

Multiple zonal jets and convective heat transport barriers in a quasi-geostrophic model of planetary cores

Céline Guervilly¹ & Philippe Cardin²

¹School of Mathematics, Statistics and Physics, Newcastle University, Newcastle upon Tyne, NE17RU, UK

²Institut des Sciences de la Terre, Université Grenoble Alpes, CNRS, 38041 Grenoble, France

May 25, 2022

Abstract

We study rapidly-rotating Boussinesq convection driven by internal heating in a full sphere. We use a numerical model based on the quasi-geostrophic approximation for the velocity field, whereas the temperature field is three-dimensional. This approximation allows us to perform simulations for Ekman numbers down to 10^{-8} , Prandtl numbers relevant for liquid metals ($\sim 10^{-1}$) and Reynolds numbers up to 3×10^4 . Persistent zonal flows composed of multiple jets form as a result of the mixing of potential vorticity. For the largest Rayleigh numbers computed, the zonal velocity is larger than the convective velocity despite the presence of boundary friction. The convective structures and the zonal jets widen when the thermal forcing increases. Prograde and retrograde zonal jets are dynamically different: in the prograde jets (which correspond to weak potential vorticity gradients) the convection transports heat efficiently and the mean temperature tends to be homogenised; by contrast, in the cores of the retrograde jets (which correspond to steep gradients of potential vorticity) the dynamics is dominated by the propagation of Rossby waves, resulting in the formation of steep mean temperature gradients and the dominance of conduction in the heat transfer process. Consequently, in quasi-geostrophic systems, the width of the retrograde zonal jets controls the efficiency of the heat transfer.

1 Introduction

Convection is the main heat transport process in the liquid cores of planets and is thought to be responsible for the generation of planetary magnetic fields. Convection is strongly affected by the rapid rotation of the planet via the action of the Coriolis force. Owing to the very low fluid viscosity, the convective flows are turbulent, although the nonlinear inertial effects are relatively weak compared with the Coriolis force. Under these conditions, and in the absence of magnetic fields, the primary dynamical balance is established between the Coriolis force and the pressure gradient and is called geostrophic balance. Geostrophic flows are invariant along the rotation axis, and so, in spherical geometry, they can only be axisymmetric and azimuthal (i.e. zonal). Convective flows, which are directed along the direction of gravity, cannot be exactly geostrophic, but nevertheless form tall columnar flows aligned with the rotation axis (Jones, 2015); such flows are commonly referred to as “quasi-geostrophic”. These columnar convective flows produce coherent Reynolds stresses that drive geostrophic zonal flows (Gilman, 1977; Busse & Hood, 1982). Stress-free boundary conditions, where boundary friction is absent, favour the emergence of strong zonal flows (e.g. Aurnou & Olson, 2001). In models with relatively small viscosity (which can be measured by the Ekman number, the ratio of the rotation period to the global viscous timescale), the zonal flows develop persistent multiple jets of alternating sign inside the tangent cylinder (e.g. Heimpel et al., 2005; Gastine et al., 2014). The observation of intense jets in geophysical and astrophysical objects (e.g. Schou et al., 1998; Porco et al., 2003; Livermore et al., 2017) has prompted much effort dedicated to their study, and in particular, their width and amplitude (e.g. Christensen, 2002; Gillet et al., 2007; Read et al., 2015; Cabanes et al., 2017). Although zonal flows (and shear flows in general) do not transport heat outwards, they strongly affect the convection because they can deflect and shear the convective flows, thereby reducing the efficiency of the heat transfer (e.g. Aurnou et al., 2008; Goluskin et al., 2014; von Hardenberg et al., 2015; Yadav et al., 2016). In the present paper, we explore the effect of intense, multiple zonal jets on the convective heat transport in turbulent rotating convection for small Ekman numbers.

The numerical modelling of turbulent rotating flows is extremely challenging as it necessitates a wide range of dynamical length and time scales. Numerical models must therefore employ Ekman numbers that are several orders of magnitude larger than those found in natural objects. However, in the absence of magnetic fields, the lengthscale of the convective flows scales with the Ekman number, at least at the linear onset of convection. The coherence of the Reynolds stresses, and hence the width and amplitude of the zonal flows, might well be affected by the convective lengthscale, and thus by the Ekman number. In order to approach turbulent rotationally-constrained convection at small Ekman numbers, we alleviate part of the computational limitations by using a quasi-geostrophic (QG) approximation that was developed by [Busse & Or \(1986\)](#) for thermal convection in the annulus geometry of [Busse \(1970\)](#) with curved boundaries. The model neglects the variations of the axial vorticity of the flow along the rotation axis, which allows to compute the velocity in two dimensions (2D). This is an important limitation to the full dynamics of rotating convection (e.g. [Calkins et al., 2013](#)), but the rationale of using this QG model is that it allows the exploration of currently inaccessible regions of the parameter space, thereby informing future three-dimensional studies. Variations of the QG model have been successfully applied in numerous studies in spherical geometry (e.g. [Cardin & Olson, 1994](#); [Morin & Dormy, 2004](#); [Calkins et al., 2012](#)). Where possible, results from these studies have been successfully benchmarked against asymptotic theories ([Gillet & Jones, 2006](#); [Labbé et al., 2015](#)), three-dimensional (3D) numerical models ([Aubert et al., 2003](#); [Plaut et al., 2008](#)), and laboratory experiments ([Aubert et al., 2003](#); [Schaeffer & Cardin, 2005](#); [Gillet et al., 2007](#)).

Following the model constructed in [Guervilly & Cardin \(2016\)](#), we use a hybrid numerical model that couples the QG velocity to a 3D implementation of the temperature in the whole sphere, in order to account for the spherical symmetry of the basic temperature background. The buoyancy driving is controlled by the temperature averaged along the direction of the rotation axis, which, contrary to QG models using a 2D temperature field ([Busse & Or, 1986](#)), is not assumed to be equal to the temperature in the equatorial plane. Solving the temperature in 3D will allow us to assess the influence of the 3D temperature on the quasi-geostrophic dynamics. This implementation is particularly appropriate to model fluids with small Prandtl numbers (the ratio of the viscosity to the thermal diffusivity) that are typical of liquid metals ($\mathcal{O}(10^{-1})$) by permitting the use of a 3D grid for the temperature that is coarser than the 2D grid used for the velocity. For simplicity, we consider only thermal convection in a full sphere without a solid inner core. The thermal convection is driven by an homogenous internal heating, which is more relevant for the early history of the Earth's core.

The existence of a so-called strong branch of convection driven by internal heating, as first suggested by the weakly nonlinear analysis of [Soward \(1977\)](#), was recently found numerically by [Guervilly & Cardin \(2016\)](#) with the hybrid QG-3D model and by [Kaplan et al. \(2017\)](#) with a fully 3D model for Ekman numbers smaller than $\mathcal{O}(10^{-7})$ and Prandtl numbers smaller than unity. The bifurcation is subcritical at the onset of convection and the strong branch is characterised by Reynolds numbers greater than 1000 near the onset and strong zonal flows. In this paper, we focus on the production of zonal flows on this strong branch of convection for $Ek \in [10^{-8}, 10^{-7}]$ and $Pr \in [10^{-2}, 10^{-1}]$.

The layout of the paper is as follows. In §2, we detail the formulation of the hybrid QG-3D model. In §3, we describe the radial dependence of the convection and zonal flows and quantify the dependence of the jet width, convective lengthscale and zonal flow velocity on the model parameters. The drift and stability of the zonal flows is discussed in §4 and their mechanism of formation in §5. The effect of the zonal flows on the heat transport is presented in §6. Finally, a discussion of the results is given in §7.

2 Mathematical formulation

We study Boussinesq thermal convection driven by internal heating in a rotating sphere. The rotation vector is $\Omega \mathbf{e}_z$, where Ω is constant. The acceleration due to gravity is radial and linear, $\mathbf{g} = g_0 r \mathbf{e}_r$. The radius of the sphere is r_o and no inner core is present. The fluid has kinematic viscosity ν , thermal diffusivity κ , density ρ , heat capacity at constant pressure C_p , and thermal expansion coefficient α , all of which are constant. We consider an homogeneous internal volumetric heating S . In the absence of convection, the static temperature profile T_s is calculated by solving the diffusive heat equation and can be written as

$$T_s(r) = T_o + \frac{S}{6\kappa\rho C_p}(r_o^2 - r^2), \quad (1)$$

where T_o is the imposed temperature at the boundary, $r = r_o$. The governing equations are solved in dimensionless form, obtained by scaling lengths with r_o , times with r_o^2/ν , and temperature with

$\nu Sr_o^2/(6\rho C_p \kappa^2)$. The system of dimensionless equations is:

$$\frac{\partial \mathbf{u}}{\partial t} + (\mathbf{u} \cdot \nabla) \mathbf{u} + \frac{2}{Ek} \mathbf{e}_z \times \mathbf{u} = -\nabla p + \nabla^2 \mathbf{u} + Ra \Theta r \mathbf{e}_r, \quad (2)$$

$$\nabla \cdot \mathbf{u} = 0, \quad (3)$$

$$\frac{\partial \Theta}{\partial t} + \mathbf{u} \cdot \nabla \Theta - \frac{2}{Pr} r u_r = \frac{1}{Pr} \nabla^2 \Theta, \quad (4)$$

where \mathbf{u} is the velocity field, p the pressure and Θ the temperature perturbation relative to the static temperature (1).

The dimensionless numbers are, the Ekman number,

$$Ek = \frac{\nu}{\Omega r_o^2}, \quad (5)$$

the Rayleigh number,

$$Ra = \frac{\alpha g_0 Sr_o^6}{6\rho C_p \nu \kappa^2}, \quad (6)$$

and the Prandtl number,

$$Pr = \frac{\nu}{\kappa}. \quad (7)$$

At $r = r_o$, the boundary condition for the velocity is no-slip and impenetrable and the temperature is fixed,

$$\mathbf{u} = \mathbf{0}, \quad \Theta = 0 \text{ at } r = r_o. \quad (8)$$

Throughout this paper, we use both spherical coordinates (r, θ, ϕ) and cylindrical polar coordinates (s, ϕ, z) . The mathematical formulation and the numerical method are described in detail in [Guervilly & Cardin \(2016\)](#), where the linearised version of the code is benchmarked against theoretical and previous numerical results at the onset of convection. The governing equations and the assumptions of the model are briefly described below.

2.1 Governing equation for the non-axisymmetric flow

To model the system of equations (2)-(4) for small Ekman and Rossby numbers, we use the quasi-geostrophic approximation to model the evolution of the velocity field (e.g. [Or & Busse, 1987](#); [Cardin & Olson, 1994](#); [Gillet & Jones, 2006](#)). The QG approximation reduces the 3D system to a 2D system by taking advantage of the small variations of the flow along z compared with variations in s and ϕ due to the rapid rotation. This approximation is only justified in the case of small slope of the boundaries, such as the [Busse \(1970\)](#) annulus. In the case of a sphere, the approximation is therefore not rigorously justified in any asymptotic limit. Consequently, our QG model is intended as a simplified model of convection in a rapidly rotating sphere that allows us to investigate unexplored regions of the parameter space. When possible, comparisons with theoretical, experimental and 3D numerical models show that the QG model correctly reproduces key properties of the full system ([Aubert et al., 2003](#); [Morin & Dormy, 2004](#); [Gillet & Jones, 2006](#); [Gillet et al., 2007](#); [Plaut et al., 2008](#)).

The QG model assumes that the fluid dynamics is dominated by the geostrophic balance, i.e. the Coriolis force balances the pressure gradient at leading order. The leading-order velocity \mathbf{u}^g is invariant along z and $\mathbf{u}^g = (u_s^g, u_\phi^g, 0)$ in cylindrical polar coordinates. By taking the z -component of the curl of the momentum equation (2) and averaging it along z , we obtain the equation for the axial vorticity, $\zeta^g = (\nabla \times \mathbf{u}^g) \cdot \mathbf{e}_z$,

$$\frac{\partial \zeta^g}{\partial t} + (\mathbf{u}^g \cdot \nabla) \zeta^g - \left(\frac{2}{Ek} + \zeta^g \right) \left\langle \frac{\partial u_z}{\partial z} \right\rangle = \nabla_e^2 \zeta^g - Ra \left\langle \frac{\partial \Theta}{\partial \phi} \right\rangle, \quad (9)$$

with

$$\nabla_e^2 A \equiv \frac{1}{s} \frac{\partial}{\partial s} \left(s \frac{\partial A}{\partial s} \right) + \frac{1}{s^2} \frac{\partial^2 A}{\partial \phi^2}, \quad (10)$$

and

$$\langle A \rangle \equiv \frac{1}{2H} \int_{-H}^{+H} A dz, \quad (11)$$

where $H = \sqrt{1 - s^2}$ is the axial distance from the spherical boundary to the equatorial plane.

The velocity \mathbf{u}^g can be described by a streamfunction ψ that models the non-axisymmetric (i.e. ϕ -dependent) components with the addition of an axisymmetric azimuthal flow,

$$\mathbf{u}^g = \frac{1}{H} \nabla \times (H\psi \mathbf{e}_z) + \overline{u_\phi^g} \mathbf{e}_\phi, \quad (12)$$

where

$$\overline{A} \equiv \frac{1}{2\pi} \int_0^{2\pi} A d\phi. \quad (13)$$

We choose this formulation for the streamfunction to account for the non-zero divergence of \mathbf{u}^g in the equatorial plane due to the return axial flow at the sloping boundaries,

$$\nabla_e \cdot \mathbf{u}^g = -\beta u_s^g, \quad (14)$$

where

$$\nabla_e \cdot \mathbf{A} \equiv \frac{1}{s} \frac{\partial s A_s}{\partial s} + \frac{1}{s} \frac{\partial A_\phi}{\partial \phi}, \quad (15)$$

and

$$\beta = \frac{1}{H} \frac{dH}{ds} = -\frac{s}{H^2}. \quad (16)$$

The axial velocity u_z is assumed to be linear in z . The third term on the left-hand side of equation (9) requires us to determine u_z at the boundary $z = \pm H$:

$$u_z|_{\pm H} = \pm \frac{1}{H} \mathbf{u} \cdot \mathbf{n}|_{\pm H} \pm \beta H u_s^g, \quad (17)$$

where the normal vector at the boundary is $\mathbf{n} = \mathbf{e}_r$. The normal component, $\mathbf{u} \cdot \mathbf{n}|_{\pm H}$, is the Ekman pumping induced by the viscous boundary layer and is determined by asymptotic methods for a linear Ekman layer, $\mathbf{u} \cdot \mathbf{n}|_{z=\pm H} = Ek^{1/2} P(s, u_s^g, u_\phi^g)$ (Greenspan, 1968). The analytical function P is derived for a spherical boundary in Schaeffer & Cardin (2005).

The numerical code solves the evolution equation of the non-axisymmetric streamfunction ψ . The no-slip and impenetrable boundary conditions imply that $\psi = \partial_s \psi = 0$ at $s = 1$. We use the regularity condition $\hat{\psi}^m = \mathcal{O}(s^m)$ at $s = 0$, where $\hat{\psi}^m(s, t)$ is the Fourier mode of azimuthal wavenumber m (see Guervilly & Cardin (2016) for more detail).

2.2 Governing equation for the zonal flow

In our model, the streamfunction ψ only describes the non-axisymmetric motions, so the axisymmetric azimuthal flows, or zonal flows, are treated separately. We take the ϕ - and z -averages of the ϕ -component of the momentum equation to obtain

$$\frac{\partial \overline{u_\phi^g}}{\partial t} + \overline{u_s^g \frac{\partial u_\phi^g}{\partial s}} + \frac{\overline{u_s^g u_\phi^g}}{s} + \frac{2}{Ek} \langle \overline{u_s} \rangle = \nabla^2 \overline{u_\phi^g} - \frac{\overline{u_\phi^g}}{s^2}. \quad (18)$$

Note that the geostrophic balance imposes that $\overline{u_s^g} = 0$. The fourth term on the left-hand side of (18) involves the z -dependent radial velocity, which corresponds to the Ekman pumping term. Using the incompressibility of the fluid, it can be shown (Aubert et al., 2003) that

$$\langle \overline{u_s} \rangle = \frac{Ek^{1/2}}{2H^{3/2}} \overline{u_\phi^g}. \quad (19)$$

The no-slip boundary condition at the outer sphere and the symmetry at the centre imply that $\overline{u_\phi^g} = 0$ at $s = 0, 1$.

2.3 Governing equation for the temperature

The dimensionless equation for the evolution of the temperature perturbation in 3D is

$$\frac{\partial \Theta}{\partial t} + \mathbf{u}^{3d} \cdot \nabla \Theta = \frac{1}{Pr} (2ru_r^{3d} + \nabla^2 \Theta). \quad (20)$$

where \mathbf{u}^{3d} is the velocity in 3D. In cylindrical polar coordinates,

$$\mathbf{u}^{3d} = (u_s^g, u_\phi^g, Ek^{1/2}zP + \beta zu_s^g). \quad (21)$$

The temperature is fixed at the outer boundary so $\Theta = 0$ at $r = 1$. At the centre of the sphere, the non-spherically symmetric components of Θ are zero by symmetry and the spherically symmetric component of $\partial_r \Theta$ is zero.

2.4 Numerical method

In the following, the superscripts g are removed for clarity. The evolution equations for ψ and $\overline{u_\phi}$ are solved on a 2D grid in the equatorial plane. A second-order finite difference scheme is implemented in radius with irregular spacing (finer near the outer boundary). In the azimuthal direction, the variables are expanded in Fourier modes. The evolution equation for the temperature is solved on a 3D grid. Similarly to the 2D grid, a finite difference scheme is used in radius. The temperature is expanded in spherical harmonics Y_l^m in the angular coordinates with l representing the latitudinal degree and m the azimuthal mode. Further detail about the numerical interpolations between the 2D and 3D grids used to compute the buoyancy term and the advection of the temperature can be found in [Guervilly & Cardin \(2016\)](#) and [Guervilly \(2010\)](#).

Table 1 gives the list of the simulations presented in this paper with some output quantities and the numerical resolutions. To quantify some of the global properties of convection, we often use the Reynolds number, which is calculated from the output of the simulations and corresponds to the time-averaged root mean square (r.m.s.) value of the velocity in dimensionless unit,

$$Re = \frac{1}{\Delta t} \int_{\Delta t} \left(\frac{3}{4\pi} \int_0^{2\pi} \int_0^1 (u_s^2 + u_\phi^2) 2H(s) ds d\phi \right)^{1/2} dt, \quad (22)$$

where u_ϕ includes the zonal velocity. We measure the convective Reynolds number, Re_c , as in equation (22) but including only the non-axisymmetric velocity. Similarly, we measure the zonal Reynolds number, Re_0 , including only the axisymmetric velocity. The integration time over which the time averages are calculated is indicated in table 1 for each simulation.

3 Structure of the convective and zonal flows and scaling of the velocity

3.1 Radial dependence of the convection

In this section, the Ekman and Prandtl numbers are fixed to $Ek = 10^{-8}$ and $Pr = 10^{-1}$. For these parameters, the stable solution is located on a strong branch of convection, which is discontinuous at the onset of convection ([Guervilly & Cardin, 2016](#); [Kaplan et al., 2017](#)). All cases presented in this paper are located on the strong branch. This branch is distinct from the weak branch of convection, which occurs for $EkPr \gtrsim \mathcal{O}(10^{-8})$ and is continuous at the onset of convection. At the onset of convection, solutions on the weak branch take the form of propagating structures that are tilted in the prograde direction. These structures are known as thermal Rossby waves and have been extensively studied in the literature (e.g. [Busse, 1970](#); [Zhang, 1992](#)). Near the onset of convection, the flows on the strong branch are starkly different and are described in detail below.

For $Ek = 10^{-8}$ and $Pr = 10^{-1}$, the nonlinear convection is maintained below the linear onset of convection (quantified by the critical Rayleigh number Ra_c), down to a value $Ra = 0.96Ra_c$ ([Guervilly & Cardin, 2016](#)). We vary the Rayleigh number from this lower value to approximately $9Ra_c$. Figure 1 shows snapshots of the radial and azimuthal velocities in the equatorial plane for $Ra/Ra_c = 0.96$, $Ra/Ra_c = 1.93$ and $Ra/Ra_c = 9.02$. In all three cases, two dynamical regions can be distinguished: an inner region, where the convection is vigorous with values of the radial velocity up to 3000 for the lowest Ra and up to 30000 for the largest Ra , and an outer region, where the radial flow has smaller amplitude and the flow has finer structures that are tilted in the prograde direction. This radial dependence of the convection, sometimes referred to as dual convection, was previously described in laboratory experiments ([Sumita & Olson, 2000](#)) and QG ([Aubert et al., 2003](#)) and 3D numerical models ([Miyagoshi et al., 2010](#)). The limit between the two regions is located around $s = 0.5$ for the lowest Ra and $s = 0.8$ for the largest Ra , so the limit moves outwards when the convection becomes more vigorous. In the inner region,

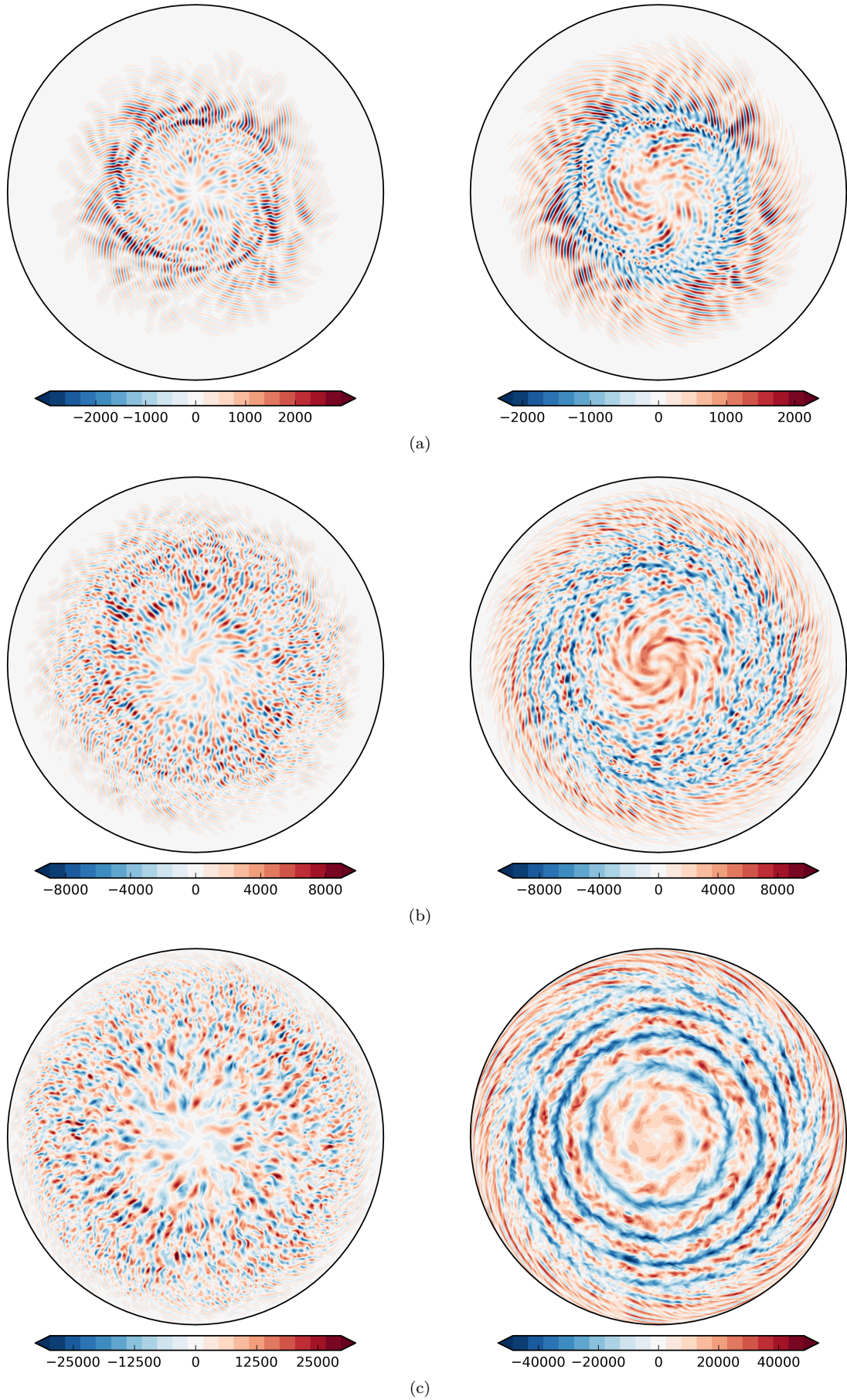


Figure 1: Snapshots of the radial velocity (left) and the azimuthal velocity (right) in the equatorial plane for $Ek = 10^{-8}$ and $Pr = 10^{-1}$ for (a) $Ra/Ra_c = 0.96$, (b) $Ra/Ra_c = 1.93$ and (c) $Ra/Ra_c = 9.02$.

Ek	Pr	Ra	Ra/Ra_c	Re_c	Re_0	(N_s^u, M_{\max}^u)	$(N_r^t, M_{\max}^t, L_{\max}^t)$	integration time
10^{-7}	10^{-1}	6×10^9	1.19	1012	445	(1100, 200)	(500, 150, 150)	3×10^5 (479)
10^{-7}	10^{-1}	1×10^{10}	1.99	2070	1110	(1100, 200)	(500, 150, 150)	3×10^5 (794)
10^{-7}	10^{-1}	2×10^{10}	3.97	3663	2994	(1200, 200)	(500, 150, 150)	10^5 (414)
10^{-7}	10^{-1}	3×10^{10}	5.96	5093	5064	(1200, 200)	(500, 150, 150)	10^4 (54)
10^{-7}	10^{-1}	4×10^{10}	7.95	6243	6840	(1200, 200)	(500, 150, 150)	10^4 (61)
10^{-7}	10^{-1}	5×10^{10}	9.94	7731	9515	(1500, 260)	(600, 180, 180)	10^4 (73)
10^{-7}	10^{-2}	1.9×10^9	1.05	5215	5710	(1000, 160)	(400, 96, 96)	2×10^4 (90)
10^{-7}	10^{-2}	3×10^9	1.65	9027	11708	(1000, 160)	(400, 96, 96)	10^4 (67)
10^{-7}	10^{-2}	4.8×10^9	2.64	11487	21834	(1200, 180)	(400, 96, 96)	10^4 (82)
10^{-7}	10^{-2}	8.5×10^9	4.68	17548	40009	(1400, 200)	(400, 96, 96)	10^4 (105)
10^{-8}	10^{-1}	7.45×10^{10}	0.96	855	243	(1600, 256)	(700, 200, 200)	2×10^6 (633)
10^{-8}	10^{-1}	7.8×10^{10}	1.01	1047	291	(1600, 256)	(700, 200, 200)	2×10^6 (785)
10^{-8}	10^{-1}	1.5×10^{11}	1.93	3393	1128	(1800, 280)	(700, 200, 200)	5×10^5 (400)
10^{-8}	10^{-1}	2×10^{11}	2.58	4876	1893	(1800, 280)	(700, 200, 200)	5×10^5 (506)
10^{-8}	10^{-1}	3×10^{11}	3.87	7108	4724	(1800, 280)	(700, 200, 200)	2×10^5 (286)
10^{-8}	10^{-1}	5×10^{11}	6.44	9920	9341	(1900, 300)	(700, 200, 200)	10^5 (191)
10^{-8}	10^{-1}	7×10^{11}	9.02	12023	13176	(2000, 320)	(750, 200, 200)	2×10^6 (4453)
10^{-8}	10^{-2}	2×10^{10}	0.68	7200	4753	(1400, 220)	(500, 128, 128)	2×10^5 (216)
10^{-8}	10^{-2}	3×10^{10}	1.01	13498	10598	(1400, 220)	(500, 128, 128)	10^5 (177)
10^{-8}	10^{-2}	5×10^{10}	1.69	23288	23309	(1500, 240)	(500, 128, 128)	4×10^4 (108)
10^{-8}	10^{-2}	8×10^{10}	2.70	33163	43609	(1600, 260)	(500, 128, 128)	5×10^4 (191)

Table 1: List of input and output parameters for all the simulations presented in the paper. Re_c and Re_0 are the convective and zonal Reynolds numbers respectively. The columns labelled (N_s^u, M_{\max}^u) and $(N_r^t, M_{\max}^t, L_{\max}^t)$ give the numerical resolutions on the 2D and 3D grids respectively. The last column gives the integration time used to compute the time averages in units of $1/\Omega$ and, in brackets, in units of a convective turnover timescale, l_c/U_c , where U_c is the r.m.s. convective velocity (equivalent to Re_c in our dimensionless units) and l_c is the convective lengthscale computed from equation (23) and averaged between $0.1 \leq s \leq 0.8$.

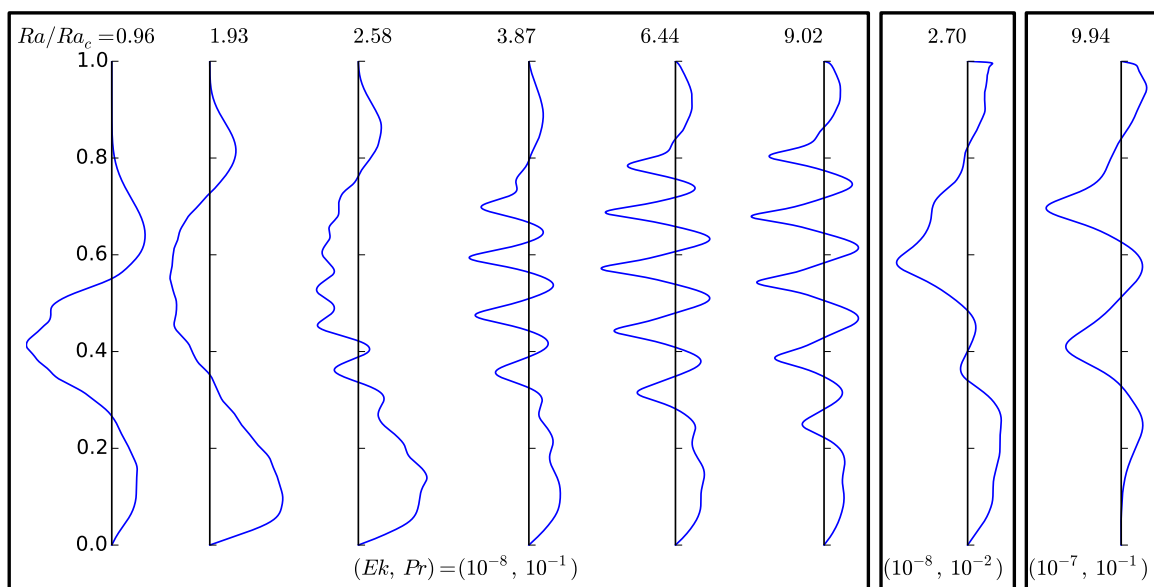


Figure 2: Radial profile of the zonal flow (time average) for different Rayleigh numbers (indicated at the top of each subplot) and Ekman and Prandtl numbers (indicated at the bottom). The vertical axis is the radius. The range of the horizontal axis is different for each subplot: the maximum of the zonal flow increases 80-fold between the smallest and largest Rayleigh numbers for $Ek = 10^{-8}$ and $Pr = 10^{-1}$.

the convective flows are strongly time dependent, especially for large Ra , and are subject to frequent nonlinear interactions. The contours of the radial velocity tend to be directed radially, contrary to the tilted contours of the outer region. For large Ra , the azimuthal lengthscales of the radial flow decreases with increasing radius. This is likely due to the increase of the slope of the boundary β with radius: the vortex stretching term in the axial vorticity equation, which depends on β , impedes the radial motion of wide vortices. The azimuthal extent of the convective flows clearly increases with Ra , which indicates the presence of an upscale energy transfer as expected in β -plane turbulence (e.g. Davidson, 2013). For all Rayleigh numbers, the radial velocity is weak in the central region because the gravity goes to zero at the centre. In the outer region, β is large and the vortex stretching term is the dominant source of the axial vorticity, so this outer region is dominated by the propagation of Rossby waves. The nonlinear interactions are weaker in this region.

For all Ra , the azimuthal flow has a visible axisymmetric (i.e. zonal) component. Figure 2 shows the time-averaged profiles of the zonal flow for different Ra . The zonal flow is prograde in the outermost region for all Ra . In the outer region dominated by Rossby waves, the Reynolds stresses due to the correlation of the velocity along the tilted contours produce a prograde jet in the outer part and a neighbouring inner retrograde jet (e.g. Busse & Hood, 1982). The behaviour of the zonal flow in the inner convective region is different depending on Ra . For the lowest Ra in figure 1, azimuthal flows appear to spiral inward from mid-radius. These flows have an axisymmetric average that is positive in the centre and negative near $s = 0.4$. The time-averaged profile of the zonal flow for this Ra has therefore three jets of alternating sign. For $Ra/Ra_c = 1.93$, the azimuthal flows consist in a multitude of meandering narrow jets. Around mid-radius, the azimuthal average of the narrow meandering jets is not well-defined. Their axisymmetric average is mostly negative because the retrograde jets have stronger amplitude. In the centre, the azimuthal flow has a clear prograde direction and is wider than the meandering jets at larger radius. For $Ra/Ra_c = 9.02$, the multiple azimuthal jets have stronger velocity than the radial flow and they do not meander so their net axisymmetric average is well-defined. The radial profile of the zonal flow shows persistent multiple jets. The central jet remains prograde and is wider than the jets located at larger radius. Overall, for $Ra > 3Ra_c$, the zonal flows develop persistent multiple jets and the innermost and outermost jets always remain prograde. The region occupied by the in-between jets becomes wider as Ra increases and the limit between inner convective region and outer Rossby wave region moves outwards. A thin viscous boundary layer can be observed on the profiles of the zonal flow of the largest Rayleigh number as the boundary condition is no-slip at $s = 1$. This thin boundary layer is well resolved in our model as the radial grid is refined near the boundary.

For large Ra , the zonal velocity is larger than the radial velocity. In this case, the radial shear exerted by the zonal flow can be faster than the vortex turnover timescale, so the zonal flow has a dominant role in the dynamics of the convective vortices. The radial flow has a smaller radial extent at the larger Ra due to the presence of the multiple zonal jets of strong amplitude. The convective structures then change from narrow in ϕ and extended in r to fatter in ϕ and shortened in r as Ra increases.

3.2 Zonal jet width and convective lengthscale

To study the influence of the zonal jets on the convective flow and vice versa, we compare the width of the zonal jet and the convective lengthscale. We expect these two lengthscales to be correlated: on the one hand, the radial shear exerted by the zonal flow on the radial velocity limits the size of the convective flow; on the other hand, the size of the most energetic convective eddies controls the width of the zonal jet by controlling the mixing length – this mechanism is discussed in detail in §5. To give an estimate of the typical lengthscale of the convection, we compute the integral lengthscale of the non-axisymmetric flow, which is defined as

$$l_c(s) = \pi s \left(\frac{\sum_{m=1}^{M_{\max}^u} E(m, s)}{\sum_{m=1}^{M_{\max}^u} m E(m, s)} \right), \quad (23)$$

where $E(m, s)$ is the time-averaged kinetic energy of a mode m of the Fourier decomposition. The axisymmetric mode ($m = 0$) is excluded from this definition. The convective lengthscale l_c and the width of the jets (denoted l_j) are plotted as a function of the radius in figure 3 for $Ra/Ra_c = 9.02$. The regions of retrograde zonal jets are indicated in grey. Both the jet width and the convective scale tend to decrease with radius in the inner convective region ($s < 0.8$). l_c takes local minimum values in the core of the jets and maximum values in the flanks of the jets where the radial shear is largest. l_c

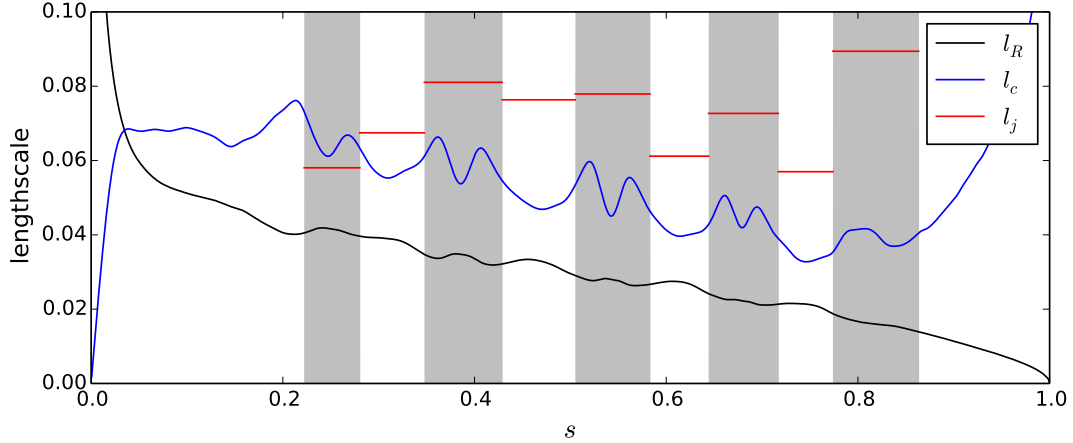


Figure 3: Radial profiles of the Rhines scale l_R , the integral scale of the convective flow l_c and the width of the jets l_j for $Ek = 10^{-8}$, $Ra/Ra_c = 9.02$ at $Pr = 10^{-1}$. The grey bands correspond to the regions where the zonal flow is retrograde.

corresponds to an azimuthal lengthscale, so this indicates that the shear from the zonal flow elongates the convective flow in the azimuthal direction as expected. The values of l_c and l_j are comparable, although the convective scale is slightly smaller than the jet width. We have thus verified that a strong correlation exists between the convective scale and the jet width.

In the framework of β -plane turbulence, a fundamental length scale of the flow is the Rhines scale (Rhines, 1975), which is given by,

$$l_R(s) = \pi \left(\frac{EkU}{2|\beta|} \right)^{1/2}, \quad (24)$$

where U is the r.m.s. velocity of the flow. In the literature, U is interpreted as either an eddy velocity, a jet velocity or a total velocity (Ingersoll & Pollard, 1982; Dritschel & McIntyre, 2008). Here we will first consider that U is the r.m.s convective velocity, and later discuss how our results differ when using the total velocity instead. Note that Ek appears in this formula due to our choice of dimensional units. The Rhines scale may be considered as the scale separating dynamical regimes dominated by either the turbulence (at smaller scales) or by Rossby waves (at larger scales). The width of the zonal jets is often thought to be closely related to the Rhines scales, although this notion has been called into question (e.g. Sukoriansky et al., 2007; Scott & Dritschel, 2012). Here we are interested in the predicted dependence of the Rhines scale on β and U (rather than on the actual value of l_R given by (24) that arbitrarily includes a factor $\pi/\sqrt{2}$) as this dependence can be compared with the lengthscales computed from our data set. We first compare the radial dependence of the Rhines scale to l_c and l_j . We plot l_R in figure 3, where we used the r.m.s value of the non-axisymmetric velocity (which varies in radius) to estimate U . In the inner convective region, the convective scale is approximately 2 times larger than the Rhines scale on average but the decreasing trends observed for each of the lengthscales is similar: between $s = 0.3$ and $s = 0.7$, l_j , l_c and l_R are all approximately divided by two. The ratio l_c/l_R is approximately constant in the inner convective region, which shows that the Rhines scale adequately predicts the radial dependence of the convective scale and the jet width.

As the Rayleigh number (and thus U) increases, the Rhines scale predicts that the most energetic convective eddies become larger. This is indeed what we observe qualitatively on the snapshots of figure 1. This increase of the convective scale should be accompanied by an increase of the jet width. Figure 2 shows that the jets indeed tend to become wider when the Rayleigh number increases. However this increase might be due to the widening of the inner convective region as it pushes the outer region outwards. Larger Ra , currently out of reach of our computational capabilities, would be necessary to observe a sizeable increase in the size of the jets.

We can extend our study on the zonal and convective lengthscales and the predictive value of the Rhines scale from the results of simulations performed at different Ek and Pr . We cannot presently run simulations at $Ek < 10^{-8}$, so this study is restricted to higher Ek , namely $Ek = 10^{-7}$. Our QG-3D model allows us to explore small Pr , so we also use results from calculations at $Pr = 10^{-2}$. The two panels on the right of figure 2 shows the zonal velocity for $(Ek, Pr) = (10^{-8}, 10^{-2})$ and $(Ek, Pr) = (10^{-7}, 10^{-1})$ at the largest Ra performed (see table 1). For $(Ek, Pr) = (10^{-7}, 10^{-1})$, the zonal flow has 5 jets of alternating sign. The zonal jets widen when the Ekman number increases if this leads to a larger r.m.s.

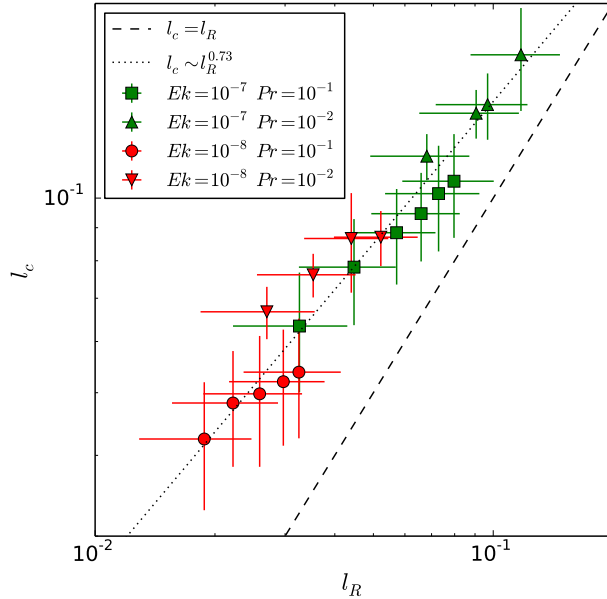


Figure 4: Convective lengthscale versus Rhines scale. Both quantities have been averaged radially in the inner convective region between $0.1 \leq s \leq 0.8$. The horizontal and vertical bars indicate the standard deviation. The dotted line indicates the best fit to all the data points.

convective velocity EkU according to the Rhines scale (24).

For $(Ek, Pr) = (10^{-8}, 10^{-2})$, the time-averaged zonal flow also has 5 alternating jets. By visual inspection of the snapshots of the velocity, it appears that meandering azimuthal flows are present in the inner region, similarly to the case $Ra = 1.93$ for $(Ek, Pr) = (10^{-8}, 10^{-1})$. This suggests that larger Rayleigh numbers would be necessary to get multiple persistent jets. However, we were not able to perform calculations at larger Ra to confirm this. Smaller values of Pr lead to larger values of the convective velocity (see table 1), and hence, to wider jets.

To compare more systematically the convective lengthscale with the Rhines scale, figure 4 shows the values of l_c versus l_R that have been radially-averaged in the inner convective region (between $0.1 \leq s \leq 0.8$), for increasing values of Ra and different Ek and Pr . Both lengthscales vary significantly with radius so we also indicate the standard deviation with vertical and horizontal bars. All the simulations are located on the strong branch of convection, which is discontinuous at the onset of convection, and l_c is always larger than the wavelength of the linear instability. The best fit to all the points is $l_c \sim l_R^{0.73(\pm 0.04)}$. Our simulations therefore indicate that the convective lengthscale increases with the convective flow speed, but it follows a power law of smaller exponent (namely $l_c \sim U^{0.37}$) than predicted by the Rhines scale (namely $l_c \sim U^{0.5}$). This result is in agreement with the work of Gastine et al. (2016) using 3D numerical simulations of rotating convection in a spherical shell with $Pr = 1$: they find that the convective lengthscale approaches the power law given by the Rhines scale when the Ekman decreases, but the exponent remains smaller than a half (0.45 for $Ek = 3 \times 10^{-7}$). Here we fitted all the points from different sets of Ekman and Prandtl numbers with one power law because, according to the Rhines scale argument, the dependence of the convective lengthscale on the parameters can be explained by a power law dependence on the flow velocity only, irrespective of the values of Ek and Pr . However there are some visible variations of the power law exponent for the different data sets, which is further indication that our data do not entirely corroborate the Rhines scale argument.

We now return to the issue of the interpretation of the velocity scale U in the Rhines scale formula (24). In our simulations, we find that the convective lengthscale approximately follows a power law $l_c \sim U^{0.28}$ when U is interpreted as the r.m.s. total velocity. The power law exponent is therefore further away from the Rhines scale prediction when using the total velocity rather than the convective velocity.

3.3 Scaling of the zonal flow velocity

To complete this section, we now discuss how the amplitude of the zonal velocity scales with the convective velocity. Figure 5a shows the evolution of the zonal Rossby number, $Ro_0 = Re_0 Ek$, as a function of the convective Rossby number, $Ro_c = Re_c Ek$, for $Ek \in [10^{-8}, 10^{-7}]$ and $Pr = [10^{-2}, 10^{-1}]$. In this section

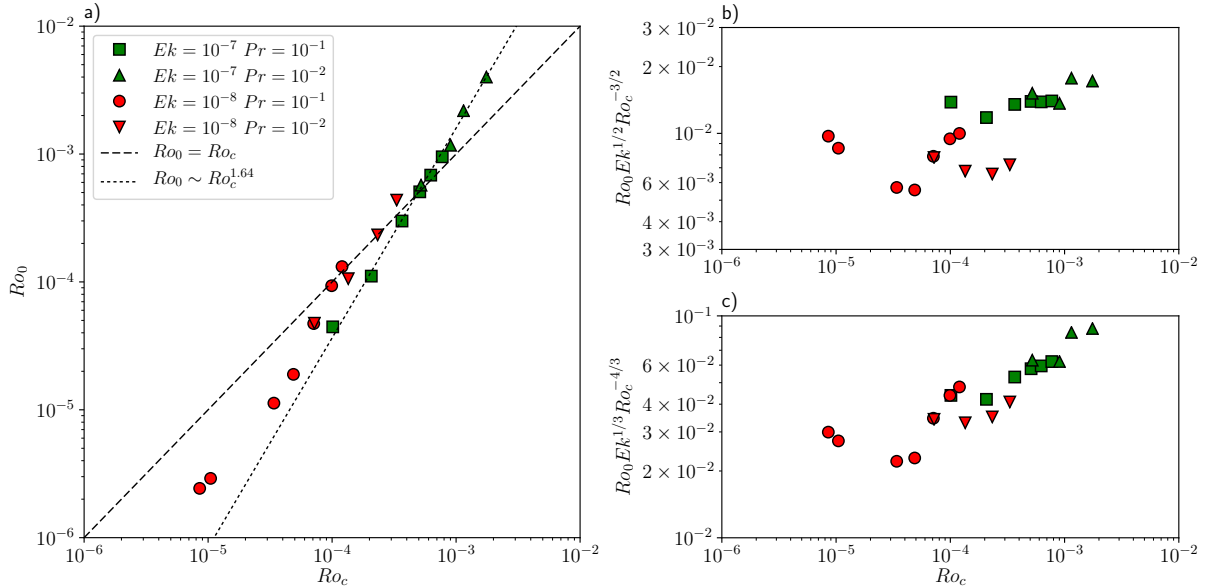


Figure 5: (a) Zonal Rossby number Ro_0 as a function of the convective Rossby number Ro_c . The dotted line shows the power law whose exponent best fits all the data points. (b)-(c) Ro_0 compensated by the power laws of (b) equation (26) and (c) equation (27) as a function of Ro_c .

we use the Rossby numbers to clarify the dependence of the velocity on the viscosity. For $EkPr \leq 10^{-9}$, the nonlinear onset of convection is subcritical (Guervilly & Cardin, 2016). In this case, the zonal and convective Reynolds numbers are discontinuous and $Re_c \gtrsim 10^3$. For each fixed value of Ek , the data points approximately fall on a straight line, indicating a power law dependence on Ro_c . The dashed line represents $Ro_0 = Ro_c$. The data points cross this line for moderate values of the Rayleigh numbers that depend on the Prandtl number: at $Ra \approx 1.5Ra_c$ for $Pr = 10^{-2}$ and $Ra \approx 6Ra_c$ for $Pr = 10^{-1}$. The zonal flows have therefore large amplitude for relatively modest values of the Rayleigh numbers when $Pr < 1$, despite the presence of the Ekman boundary friction in our model. They reach an amplitude comparable to the amplitude of the convective flows for smaller Ra as Pr is decreased. In this sense, lower Pr is favourable for the zonal flows.

A scaling law for the zonal flow amplitude can be obtained by considering that the dominant force balance in the zonal velocity equation (18) is established between the nonlinear interactions of the convective velocities and the friction in the Ekman layer. This is consistent with measurements of the contributions to the zonal energy budget in our simulations. For instance, in the case $Ek = 10^{-8}$, $Pr = 10^{-1}$ and $Ra/Ra_c = 9.02$, we measured that the boundary friction accounts for 90% of the total viscous dissipation of the axisymmetric flow. In terms of scaling arguments, this balance implies

$$Ro_0 \sim Ek^{-1/2} \frac{Ro_c^2}{l_c}. \quad (25)$$

Using the scaling $l_c \sim Ro_c^{0.37}$ deduced from our data in §3.2, we obtain the scaling $Ro_0 \sim Ro_c^{1.63}$. The best fit to all the data points in figure 5a is $Ro_0 \sim Ro_c^{1.64(\pm 0.04)}$. This agreement is not surprising because all the global quantities are calculated from the same data set, but it shows that our measurements of the global values of the convective lengthscales and the velocities are consistent and that equation (25) is suitable to scale the zonal flow velocity.

It is interesting to compare the observed scaling of the zonal velocity with predictive scaling laws based on physical arguments that have been derived in the literature (e.g. Aubert et al., 2001). To do so, we need to examine possible scaling arguments for l_c . Considering first that l_c scales with the Rhines scale (24), $l_c \sim Ro_c^{1/2}$, gives

$$Ro_0 \sim Ek^{-1/2} Ro_c^{3/2}. \quad (26)$$

The exponent 3/2 is in good agreement with the results of the 3D numerical simulations of Kaplan et al. (2017) for $Ek \in [10^{-7}, 10^{-6}]$ and $Pr \in [3 \times 10^{-3}, 10^{-1}]$.

Gillet et al. (2007) proposed an alternative scaling for l_c obtained by using the zonal velocity as a typical flow velocity in the Rhines scale. This gives $l_c \sim Ro_0^{1/2}$, and so,

$$Ro_0 \sim Ek^{-1/3} Ro_c^{4/3}. \quad (27)$$

Gillet et al. (2007) found that this scaling law provides a good fit for their numerical data obtained with a QG model at $Ek = \mathcal{O}(10^{-6})$ and $Pr = 0.025$.

Finally, we can consider $l_c \sim Ek^{1/3}$, which corresponds to the scaling of the azimuthal lengthscale of the linear convective instability (Jones et al., 2000). This estimate is obviously not satisfactory because the convective lengthscale must increase with the Rayleigh number as shown in figure 1 and figure 4. For this estimate, we deduce the scaling law

$$Ro_0 \sim Ek^{-5/6} Ro_c^2. \quad (28)$$

The power law (26) provides the closest exponent to our data best fit and is based on plausible physical arguments. By contrast, the power law (28) is too steep and the dependence of the prefactor on Ek is much weaker in the data. The power law (27) requires a much stronger dependence of the convective lengthscale on Ro_c (namely $l_c \sim Ro_c^{2/3}$) than observed. Figures 5b and c show the dependence of Ro_0 compensated by the power laws (26) and (27), respectively, on Ro_c . The data points compensated by the power law (26) align on a plateau, confirming that the exponent of this power law provides a reasonable agreement with our data.

The prefactor of the power law (26) predicts that a decrease of Ek by a decade should lead to an increase of Ro_0 by approximately a factor 3. The dependence on the Ekman number cannot be estimated accurately from our data points as they only sample one decade of Ek . Figure 5b tentatively suggests that the power law (26) does not entirely explain the dependence on the Ekman number: in our simulations, Ro_0 only increases by approximately a factor 2 when Ek decreases from 10^{-7} to 10^{-8} .

4 Drift and stability of the zonal jets

In the rest of the paper, we only consider simulations run at $Ek = 10^{-8}$ and $Pr = 10^{-1}$, where we obtain the largest number of zonal jets. The zonal flows have a strong influence on the convective flows, and hence on the heat transport as we will discuss in §6, so it is important to discuss the persistence of the zonal jets. In this section, we examine the stability of the jets.

Using a QG model of thermal convection, Rotvig (2007) shows that zonal jets drift inwards provided that the slope β has a significant dependence on radius, while QG models with constant β produce multiple jets that do not drift (e.g. Jones et al., 2003). Rotvig showed that the drift also occurs in a 3D spherical model, so this effect is not restricted to QG models. The drift rate is found to increase with β and with the Rayleigh number. The drift of zonal flows is also observed in the rotating turntable experiment of Smith et al. (2014). In the experiment, β is positive and the drift is observed outwards. These studies thus indicate that the direction of the zonal jet drift is related to the sign of β .

Figure 6 shows the space-time diagram of the zonal velocity for $Ra/Ra_c = 0.96$ and $Ra/Ra_c = 9.02$. For $Ra = 0.96$, the middle retrograde zonal jet drifts inwards periodically. In our system $\beta < 0$ so this inwards migration of the zonal flows is in agreement with the work of Rotvig (2007) and Smith et al. (2014).

For $Ra/Ra_c = 9.02$, the picture is completely different. For $s > 0.4$ the zonal jets do not drift and the standard deviation of their amplitude is of the order of 2000 (compared with a mean amplitude of approximately 30000) over the course of the simulation. However at radius $s < 0.4$, the central prograde jet and its retrograde neighbour drift outwards. The retrograde jet initially forms around $s = 0.2$ and eventually merges with the retrograde jet located at $s \approx 0.35$, closing off the prograde jet in the process. This sequence is not quite periodic and takes between 5 to 20 zonal turnover timescale (based on the time- and volume-averaged zonal velocity). The central region of the equatorial plane has the smallest values of β and $d\beta/ds$, so the direction and the location of the drift indicates that this mechanism is different from the inward drift observed for smaller Ra and large β .

The drift might be related to instabilities of the prograde jets near the centre, where β goes to zero. The Rayleigh-Kuo criterion states that a necessary condition for the barotropic instability of a shear flow in a inviscid Boussinesq fluid is that the quantity $\Delta = 2\beta Ek^{-1} - d\bar{\zeta}/ds$, where $\bar{\zeta} = d\bar{u}_\phi/ds + \bar{u}_\phi/s$, changes sign at some radius (Kuo, 1949). This indicates that large slopes have a stabilising effect on the zonal flow, so it is plausible that prograde zonal flows near the centre are unstable. The criterion is valid for an inviscid fluid, so it only provides an indication of the zonal flow stability for small Ekman numbers. Nevertheless, Guervilly et al. (2012) showed that the threshold of the instability obtained with numerical simulations is in good quantitative agreement with the Rayleigh-Kuo criterion for $Ek < 10^{-7}$. As well as calculating the quantity Δ in the time series of $Ra/Ra_c = 9.02$, we also compute the product

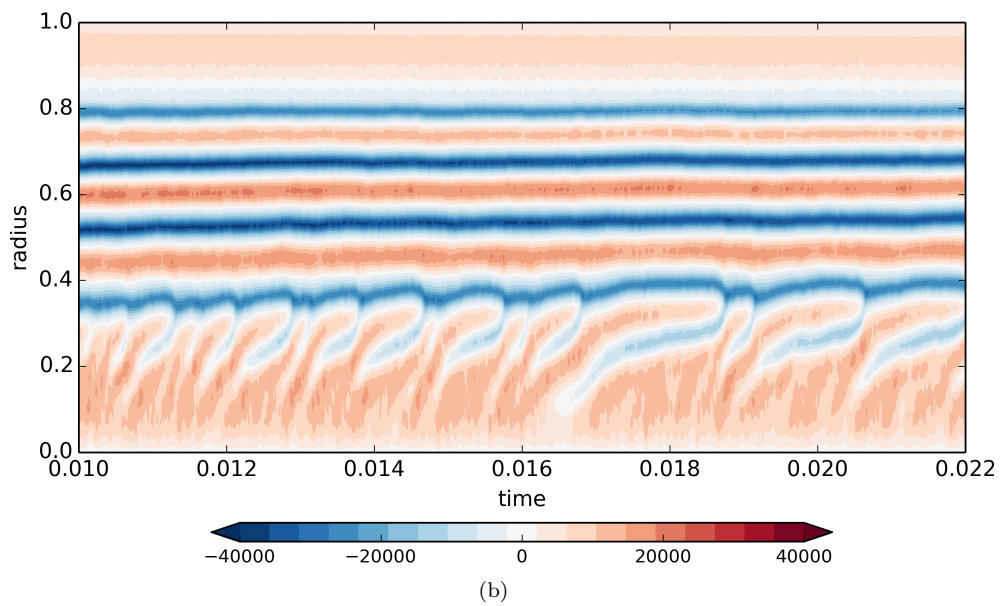
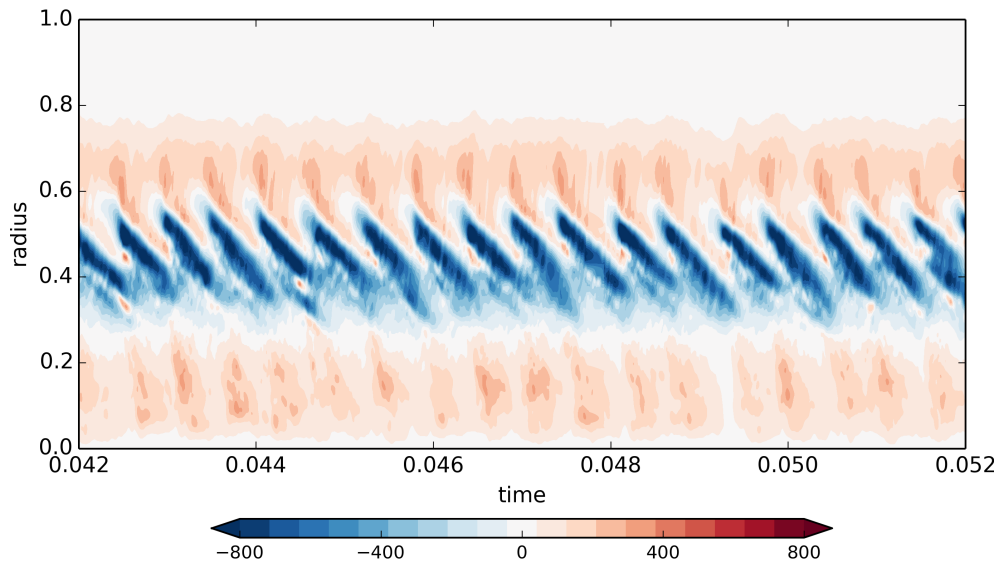


Figure 6: Space-time diagram of the zonal velocity for (a) $Ra/Ra_c = 0.96$ and (b) $Ra/Ra_c = 9.02$ ($Ek = 10^{-8}$ and $Pr = 10^{-1}$). The time interval corresponds to (a) 10^6 rotation periods and 317 convective turnover timescales (as defined in table 1) and (b) 1.2×10^6 rotation periods and 2672 convective turnover timescales.

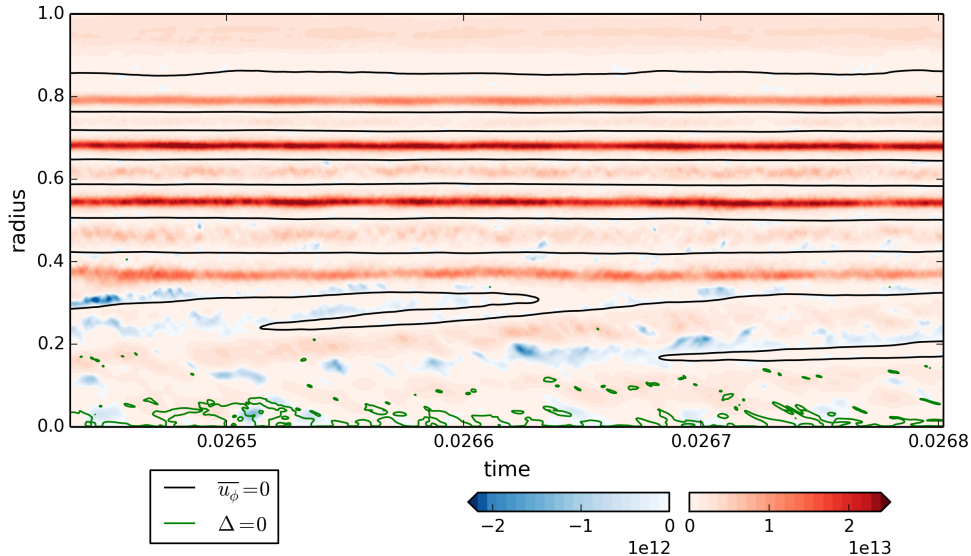


Figure 7: Space-time diagram of R (colour) for $Ra/Ra_c = 9.02$ ($Ek = 10^{-8}$, $Pr = 10^{-1}$). The isocontours $\overline{u_\phi} = 0$ and $\Delta = 0$ have been represented in black and green respectively. The time interval corresponds to 3.5×10^4 rotation periods and 78 convective turnover timescales (as defined in table 1).

of $\overline{u_\phi}$ with the zonal average of the eddy momentum flux convergence given in the zonal velocity equation (18),

$$R = - \left(u'_s \frac{\partial u'_\phi}{\partial s} + \frac{u'_s u'_\phi}{s} \right) \overline{u_\phi}, \quad (29)$$

where the prime denotes the non-axisymmetric velocity component. R is the only source of energy of the zonal flow, so we expect this term to be positive when the eddies feed energy into the zonal velocity. Figure 7 shows the space-time diagram of R (colour), where the isocontours of $\overline{u_\phi} = 0$ (black line) and $\Delta = 0$ (green line) have been superposed. In the central region, R is negative in the inward flank of the drifting prograde jet, meaning that the zonal flows lose energy to the non-axisymmetric flows there. The instability criteria (i.e. $\Delta > 0$) is violated near the centre where β is small and in a few places in the drifting prograde jet. This indicates that this prograde jet might be marginally stable, leading to a transfer of energy from the zonal flow to non-axisymmetric flows. As the zonal flow loses energy in the inward flank of the prograde jet, we expect the fluid parcels located there to move outwards to conserve their angular momentum. This mechanism could explain why the prograde jet moves outwards, and by doing so, pushes the neighbouring retrograde jet outwards.

5 Dynamical difference between retrograde and prograde jets

We now discuss the mechanism of formation of persistent zonal flows based on the extensive literature on the subject, particularly in the context of the ocean and atmosphere dynamics (e.g. Vallis, 2006). In our simulations, retrograde zonal flows are faster and sharper than the rounded prograde zonal flows. This asymmetry is indicative of an important dynamical difference between the two types of zonal jets, related to their formation mechanism and to the sign of β . The asymmetry is also observed in 3D models of rotating spherical convection (e.g. Heimpel & Aurnou, 2007; Gastine et al., 2014) and in QG models with constant β (e.g. Teed et al., 2012). In the 3D simulations, the multiple zonal jets emerge inside the tangent cylinder, where β is positive, so the prograde flows are faster and sharper than the retrograde flows.

In quasi-geostrophic flows, the zonal flows are directly related to the distribution of potential vorticity (PV) (e.g. McIntyre, 2003). In our system, the equation for the evolution of the potential vorticity, q , is

$$\frac{\partial q}{\partial t} + \mathbf{u} \cdot \nabla q = D + F, \quad (30)$$

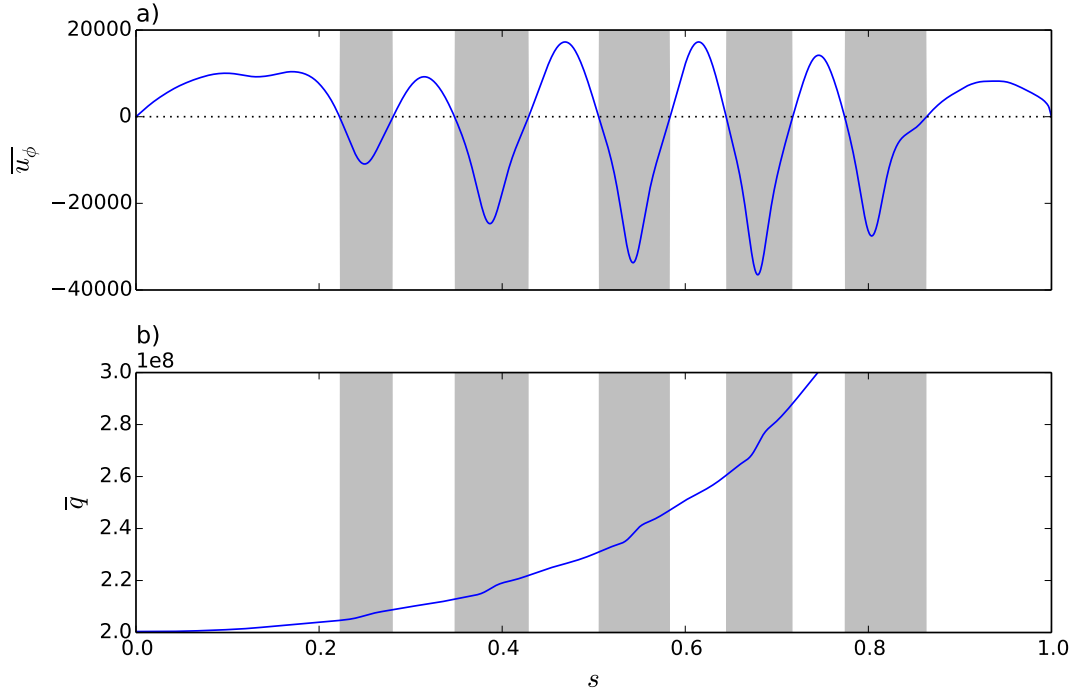


Figure 8: Radial profile of (a) the zonal velocity and (b) the axisymmetric potential vorticity (time averages) for $Ra/Ra_c = 9.02$ ($Ek = 10^{-8}$, $Pr = 10^{-1}$). The grey bands correspond to the regions where the zonal flow is retrograde.

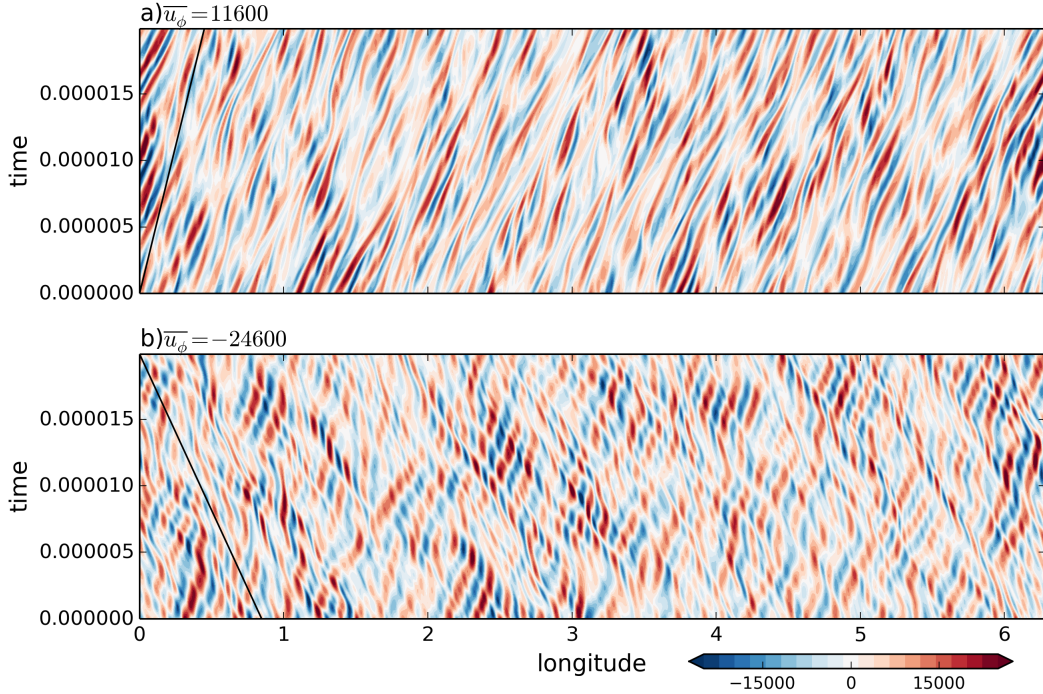


Figure 9: Hovmöller map (longitude-time) of the radial velocity u_s at a fixed radius: (a) $s = 0.51$ in a prograde jet ($\overline{u}_\phi = 11600$) and (b) $s = 0.58$ in a retrograde jet ($\overline{u}_\phi = -24600$) for $Ra/Ra_c = 6.44$ ($Ek = 10^{-8}$, $Pr = 10^{-1}$). The solid black line shows the drift due to the advection by the zonal velocity. The time interval corresponds to 2000 rotation periods and 4 convective turnover timescales (as defined in table 1).

where

$$q = \frac{\zeta + 2Ek^{-1}}{H}, \quad (31)$$

D represents the dissipation terms from the boundary and the bulk and F the buoyancy source. ζ includes the axisymmetric and non-axisymmetric components of the vorticity. In the absence of buoyancy sources and dissipative effects, q is a materially invariant scalar so it tends to be locally homogenised by the turbulence. The zonal flows appear as a consequence of the mixing of PV with

$$\overline{u_\phi}(s) = \frac{1}{s} \int_0^s s' \bar{\zeta} ds' = \frac{1}{s} \int_0^s s' (H\bar{q} - 2Ek^{-1}) ds'. \quad (32)$$

In a sphere (where H decreases with s , i.e. $\beta < 0$), regions of weak PV gradients correspond to prograde zonal jets, while regions of strong PV gradient correspond to retrograde zonal jets. The PV distribution controls the quasi-geostrophic dynamics and, in particular, the propagation of Rossby waves. The equation for linear Rossby waves is

$$\frac{\partial \zeta'}{\partial t} + u_s H \frac{d\bar{q}}{ds} = 0, \quad (33)$$

where $\zeta' = \zeta - \bar{\zeta}$ and

$$\frac{d\bar{q}}{ds} = \frac{d\bar{\zeta}/H}{ds} - \frac{2\beta}{EkH}. \quad (34)$$

The restoring mechanism of the Rossby waves is therefore stronger in the retrograde jets than in the prograde jets. A strong mixing leads to the formation of a staircase of PV, i.e. a succession of regions of homogeneous PV separated by regions of steep PV gradients (e.g. [Scott & Dritschel, 2012](#)). This occurs because perturbations to strong PV gradients are radiated as Rossby waves, an effect referred to as Rossby wave elasticity ([McIntyre, 2008](#)). Perturbations are therefore inhibited in the regions of strong PV gradients, while they are intensified in regions of weak PV gradients. This leads to a feedback mechanism that further steepens the gradients of PV ([Dritschel & McIntyre, 2008](#)). In a sphere, the relation between PV and zonal flows (32) implies that wide regions of weak PV gradients appear as large rounded prograde jets, whereas narrow regions of steep PV gradients appear as sharp retrograde jets.

The radial profile of the axisymmetric potential vorticity is plotted in figure 8 for $Ra/Ra_c = 9.02$. In the range $s \in [0, 0.8]$, the succession of weak and steep PV gradient regions is visible and forms a relatively mild PV staircase for this value of Ra . Larger Ra are required to obtain well mixed PV regions and a better formed staircase profile. The asymmetry of the jets is clearly visible in our simulations but retrograde jets are not particularly narrower than the prograde jets. This is because the chosen delimitation of the jets ($\overline{u_\phi} = 0$) is, somewhat arbitrarily, defined with respect to the planetary rotation. The profile of \bar{q} shows that the regions of steep PV gradients (which correspond to the cores of the retrograde jets) are in fact much narrower than the regions of weak PV gradients. Another characteristic of the zonal flow is the robustness of the prograde jet at the centre in all our simulations: this is well explained by the mixing in the central region that leads to a local increase of q . The PV mixing mechanism therefore provides a good explanation for the most notable features of the zonal flows observed in our simulations. Nevertheless, we note that alternative – although not mutually exclusive – mechanisms for the formation of persistent zonal flows have been put forward in the literature, such as resonant triad interactions (e.g. [Pedlosky, 1987](#)).

The PV distribution indicates that the non-axisymmetric dynamics inside the retrograde jets might be dominated by Rossby waves. Assuming for simplicity $\zeta' = -\nabla_e^2 \psi$ (see equation 12), the dispersion relation of the Rossby waves is

$$\omega = H \frac{d\bar{q}}{ds} \frac{k_\phi}{|\mathbf{k}|^2}, \quad (35)$$

where ω is the frequency of the wave and $\mathbf{k} = (k_s, k_\phi)$ is the wavenumber vector. Consequently, the azimuthal phase velocity, v_p , and azimuthal group velocity, v_g , of the Rossby waves are

$$v_p = H \frac{d\bar{q}}{ds} \frac{1}{|\mathbf{k}|^2}, \quad v_g = H \frac{d\bar{q}}{ds} \frac{k_s^2 - k_\phi^2}{|\mathbf{k}|^4}. \quad (36)$$

In our system, the gradient of \bar{q} is positive so the Rossby waves always have a positive azimuthal phase speed. To determine whether Rossby waves are present in the retrograde jets, we can track the direction of the azimuthal drift of the velocity patterns. Figure 9 shows the Hovmöller map (longitude-time) of the radial velocity u_s at a fixed radius in a prograde jet ($\overline{u_\phi} = 11600$) and in a retrograde jet ($\overline{u_\phi} = -24600$).

The solid black line represents the azimuthal drift due to the advection by the zonal velocity at this radius, $\Delta t = s\Delta\phi/\bar{u}_\phi$. In the prograde jet, the radial velocity structures move in the prograde direction at a rate that is consistent with the advection by the zonal velocity, and even faster for some structures. In the retrograde jet, the radial velocity patterns mainly move in the prograde direction. These patterns must therefore correspond to Rossby waves. The amplitude of the patterns of u_s is modulated as they move in the prograde direction. These modulations appear on neighbouring patterns and seem to travel in the retrograde direction. This observation is consistent with Rossby waves for which $k_s < k_\phi$ so their azimuthal group velocity is negative. In the frame of reference (i.e. rotating at the rotation rate Ω), the Rossby waves move at a velocity $v_p + \bar{u}_\phi$. From figure 9b, we estimate that this velocity is approximately 20000, which gives $v_p \approx 45000$. By using the local value of the gradient of \bar{q} at this radius, we find that $|\mathbf{k}|^2 \approx 84$ from eq. (36). From figure 9b we estimate that the azimuthal wavenumber is $k_\phi = m/s \approx 70$, and so, we deduce that $k_s \approx 46$. This result is consistent with a negative azimuthal group velocity.

We might expect that the dynamical difference between prograde and retrograde jets affects the temperature distribution because the Rossby waves might modify the transport properties of the flow. We study this problem in the next section.

6 Effect of the zonal flows on the heat transport

First, we can assess the effect of the zonal flow on the amplitude of the radial flow by comparing the profile of the zonal velocity to the radial profile of the r.m.s radial velocity, u_s^* , which is calculated as

$$u_s^*(s) = \frac{1}{\Delta t} \int_{\Delta t} \left(\frac{1}{2\pi s} \int_0^{2\pi} u_s^2(s, \phi, t) s d\phi \right)^{1/2} dt. \quad (37)$$

Figure 10a shows these profiles for $Ra/Ra_c = 9.02$. The zonal flow (black line) is plotted according to the left axis and u_s^* (blue line) is plotted according to the right axis. Both profiles are time-averaged. In the inner convective region ($s \lesssim 0.8$), the local maxima of u_s^* correlates well with the extrema of \bar{u}_ϕ (the cores of the jets), i.e. the zeros of the radial shear $|\partial_s \bar{u}_\phi|$, while the local minima of u_s^* correlates with maxima of $|\partial_s \bar{u}_\phi|$ (the flanks of the jets). The reduction of u_s^* in the flank of a jet can reach 30% of its value in the core of the neighbouring jets. The radial velocity is therefore impeded by the radial shear and maximised in the cores of jets, irrespective of their sign. Thus the dynamical difference between prograde and retrograde jets cannot be directly diagnosed on this profile.

To determine how the temperature field is affected by the zonal flows, figure 11a shows a meridional slice of the axisymmetric temperature, $\bar{T} = \bar{\Theta} + T_s$, averaged in time for the same simulation. The isotherms have an ellipsoidal shape which is elongated towards the equator. To complement this figure, the radial profiles of the axisymmetric temperature along the rotation axis, $\bar{T}(\theta = 0)$, and in the equatorial plane, $\bar{T}(\theta = \pi/2)$, are plotted in figure 10b. In the equatorial plane, the temperature has a flatter profile than along the rotation axis for $s < 0.8$, which explains the ellipsoidal shape of the isotherms. The thermal boundary layer is more pronounced in the equatorial plane. Nevertheless it remains thick (much thicker than the Ekman layer) because $Pr < 1$ and the Rayleigh number is moderate. The disparity between the temperature along the axial and equatorial directions is due to preferential direction of the convective flows in rapidly rotating convection. This effect is also observed in 3D models (e.g. Zhang, 1991; Yadav et al., 2016), but is amplified here by the use of a quasi-geostrophic model.

On top of their ellipsoidal shape, the isotherms also have undulations of small amplitude. These undulations are located at the same distance from the rotation axis for each isotherm so they are likely due to the presence of zonal flows. This causal link is visible in figure 10b where we use the radial profile of $\bar{T}(\theta = \pi/2)$ as a proxy for the z -averaged axisymmetric temperature. The temperature profile is relatively flat in the prograde zonal jets. By contrast it is significantly steeper in the core of the retrograde jets. This indicates that the mean temperature is affected by the PV distribution: in the core of the retrograde jets, the inhibition of the turbulence and the dominance of the Rossby waves imply that the temperature cannot be efficiently homogenised.

This effect can be quantified by measuring the heat fluxes carried by convection and conduction through the system. In the steady state, the volume average of the heat equation implies that

$$\frac{1}{\bar{S}} \int_{\bar{S}} (F_{cv} + F_{cd}) d\mathcal{S} = F_s, \quad (38)$$

where the convective heat flux is

$$F_{cv} = \Theta u_r, \quad (39)$$

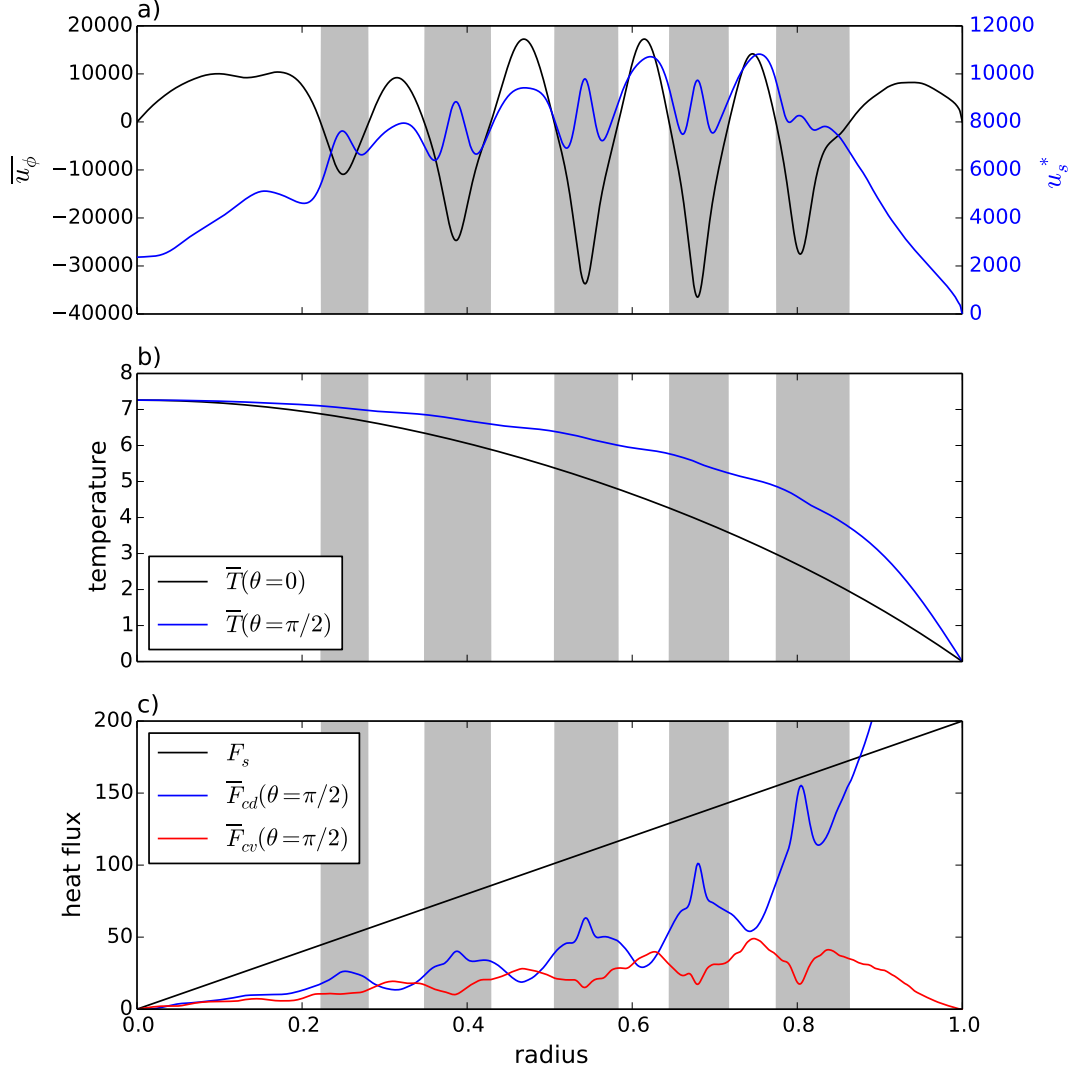


Figure 10: Radial profile of (a) the zonal velocity (black line) and the r.m.s radial velocity (blue), (b) the axisymmetric temperature along the rotation axis (black) and in the equatorial plane (blue), (c) the static heat flux (black), the conductive heat flux in the equatorial plane (blue) and the convective heat flux in the equatorial plane (red). All the quantities have been time-averaged. The grey bands correspond to the regions where the zonal flow is retrograde. The parameters are $Ra/Ra_c = 9.02$, $Ek = 10^{-8}$ and $Pr = 10^{-1}$.

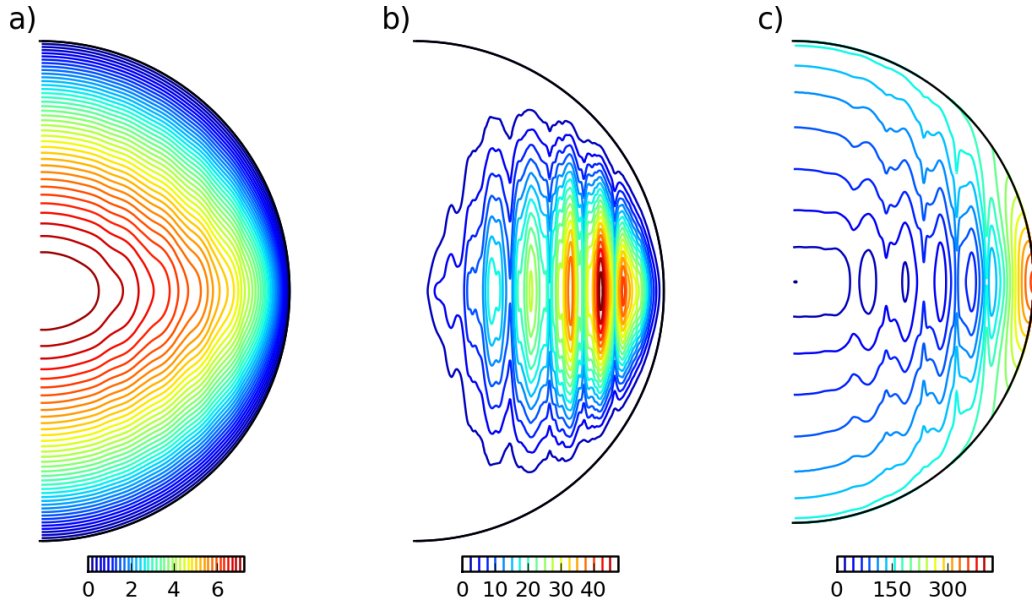


Figure 11: Meridional cross-section of the axisymmetric average of (a) the temperature $\bar{T} = \bar{\Theta} + T_s$, (b) the convective heat flux \bar{F}_{cv} , and (c) the conductive heat flux \bar{F}_{cd} . All the quantities have been time-averaged. Same parameters as figure 10.

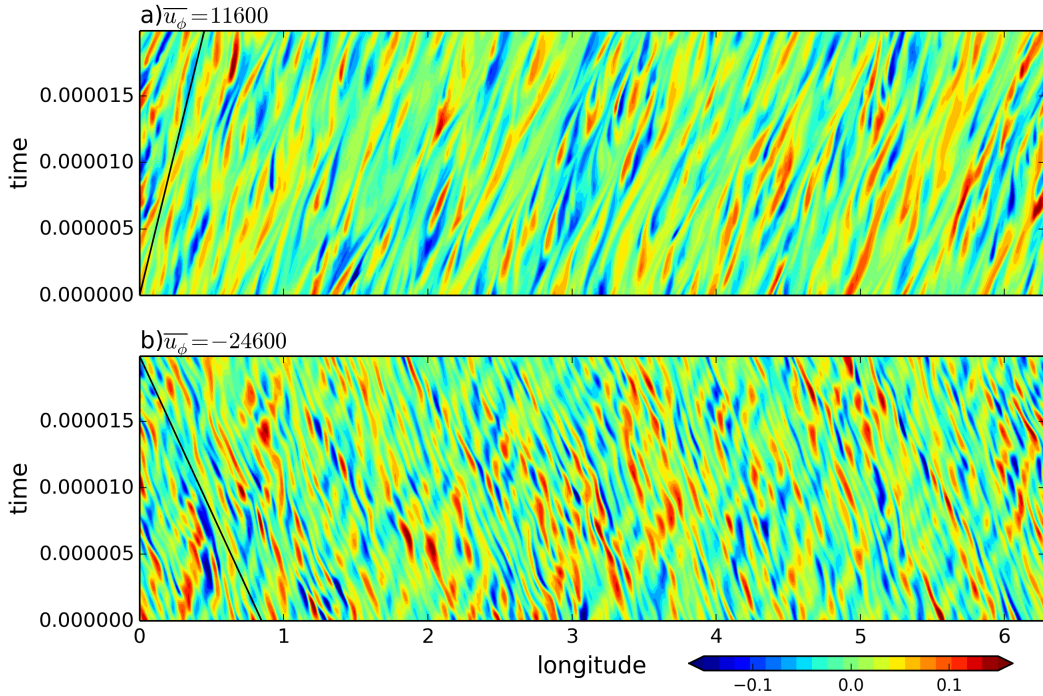


Figure 12: Hovmöller map of the non-axisymmetric temperature perturbation, Θ' , at a fixed radius: (a) $s = 0.51$ in a prograde jet and (b) $s = 0.58$ in a retrograde jet for the same parameters as figure 9. The solid black line shows the drift due to the advection by the zonal velocity. The time interval corresponds to 2000 rotation periods and 4 convective turnover timescales (as defined in table 1).

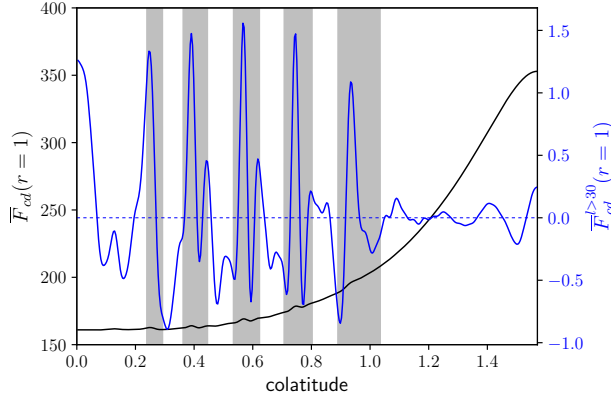


Figure 13: Latitudinal profile of the axisymmetric heat flux (black line) from the North pole to the equator at the outer boundary $r = 1$ for $Ek = 10^{-8}$, $Pr = 10^{-1}$ and $Ra/Ra_c = 9.02$. The blue line shows the axisymmetric heat flux where the spherical harmonics coefficient of degrees $l \leq 30$ have been filtered out and is plotted according to the right axis. The grey bands correspond to the regions where the zonal flow is retrograde.

the conductive heat flux,

$$F_{cd} = -\frac{1}{Pr} \frac{\partial T}{\partial r}, \quad (40)$$

the static heat flux,

$$F_s = -\frac{1}{Pr} \frac{dT_s}{dr} = \frac{2}{Pr^2} r, \quad (41)$$

and \mathcal{S} is a spherical surface. Figure 11 shows the meridional slices of the axisymmetric averages of the convective heat flux, \overline{F}_{cv} , and of the conductive heat flux, \overline{F}_{cd} . The fluxes are time-averaged. Both fluxes have a banded structure aligned with z . The convective heat flux is mainly concentrated around the equatorial plane and is weak near the axis. The conductive heat flux is maximum near the equator. For this simulation at $Pr = 10^{-1}$, the conduction carries a larger part of the heat than the convection in most of the domain, despite the large values of the radial velocity (of the order of 10^4).

The thermal contrast between prograde and retrograde jets can be clearly observed in the profiles of the axisymmetric heat fluxes in the equatorial plane shown in figure 10c. For comparison, the static heat flux F_s is also shown. Note that the profile of \overline{F}_{cv} and \overline{F}_{cd} at a given latitude are not representative of the spherical averages so their sum is not equal to F_s at each radius. The local maxima of the convective flux are located in the prograde zonal jets. The decrease of the convective flux matches the decrease of u_s^* in the shear layers. However the convective flux systematically reaches minima in the core of the retrograde jets while the radial velocity recovers there. The conductive flux is boosted in the shear layers, but even more so in the retrograde jets, where it is much larger than the convective flux. The balance between the thermal processes is very different in the prograde and retrograde jets: the prograde jets are regions where about half of the heat is carried by the convection and the temperature is fairly uniform, whereas most of the heat is carried by the conductive flux in the retrograde jets. This occurs despite high values of the r.m.s radial velocity in the retrograde jets, so the radial flow must not be well correlated with the temperature perturbation in these regions. Figure 12 show the Hovmöller map for the non-axisymmetric temperature perturbation, $\Theta' = \Theta - \overline{\Theta}$, for the same parameters and radius as figure 9. In both prograde and retrograde jets, the temperature perturbation drifts in the direction of the zonal flow with a drift rate consistent with the advection by the zonal velocity. In the core of the retrograde jets, which are dominated by the propagation of Rossby waves, the radial velocity and temperature perturbation are visibly not well correlated. The inefficiency of the Rossby waves at transporting heat outwards explains the weak convective heat flux there. In the prograde jet, Θ' is well correlated with u_s , which is consistent with the high convective heat flux.

In summary, our results show that the core of the retrograde jets – and not only the regions of intense shear – act as primary bottlenecks to the convective heat transport.

7 Discussion

In this paper, we have studied the convective structures and zonal flows that form in rotating thermal convection for values of the Prandtl number relevant for liquid metals ($Pr = \mathcal{O}(10^{-1})$) and low Ekman

($Ek = \mathcal{O}(10^{-8})$) and Rossby numbers ($Ro_c < 10^{-2}$). In order to reach low values of the Ekman number, we have used a hybrid numerical model that couples a quasi-geostrophic approximation for the velocity to a 3D temperature field. Convection is driven by internal heating in a full sphere geometry. The model includes Ekman pumping to mimic no-slip boundary conditions. We focus on the intense zonal flows that emerge on the strong branch of convection, which was described by [Guervilly & Cardin \(2016\)](#) using the same hybrid QG-3D model and by [Kaplan et al. \(2017\)](#) in a fully 3D model. Persistent multiple zonal jets of alternating sign form due to the mixing of potential vorticity and exert a strong feedback on the convection. An upscale energy transfer takes place and the integral convective lengthscale increases with the vigour of the convection. The convective lengthscale and the zonal jet width are closely related: the radial shear exerted by the zonal flow on the radial velocity limits the size of the convective eddies, while the typical mixing length of the potential vorticity depends on the size of the most energetic convective eddies. The convective lengthscale varies radially in agreement with the Rhines scale ([Rhines, 1975](#)), i.e. as the square root of β , where β measures the slope of the boundaries. However the convective scale increases more slowly with the convective speed (following a power law of exponent 0.37) than predicted by the Rhines scale (power law of exponent 0.5).

In our quasi-geostrophic model, convection carries heat mostly in the direction perpendicular to the rotation axis. We have shown that the principal barrier to this convective heat transport is located in the cores of the retrograde zonal jets. This is due to the formation of a staircase of potential vorticity: steep and weak gradients of the potential vorticity correspond to retrograde and prograde zonal jets, respectively. The steep PV gradients inhibit the eddies and favour the propagation of Rossby waves, which are inefficient at carrying heat outwards. The occurrence of eddy-transport barriers associated with strong zonal jets is well-documented in the atmospheric dynamics context ([Dritschel & McIntyre, 2008](#)). In our simulations, these barriers lead to the steepening of the mean temperature gradient in the core of the retrograde jets, and there, the heat is largely carried by conduction. The unfavourable effect of the shear layer in the flanks of the zonal jets on the convective heat transport is secondary by comparison. To illustrate the thermal signature of the retrograde jets at the surface, we plot in figure 13 the latitudinal profile of the axisymmetric heat flux at $r = 1$. The most noticeable feature is that the heat flux is maximal at the equator, which is expected as the convective transport is largely perpendicular to the rotation axis, and is also observed in 3D models (e.g. [Zhang, 1991](#); [Yadav et al., 2016](#)). This enhanced heat transport in the equatorial regions compared with the polar regions is used in a number of models of the Earth’s inner core growth to explain the observed seismic anisotropy (e.g. [Yoshida et al., 1996](#); [Deguen & Cardin, 2009](#)). Of greater interest here are the more subtle variations of the surface heat flux at higher latitudes: the cores of the retrograde jets are characterised by local maxima of the (conductive) surface heat flux. This occurs because the axisymmetric temperature gradient is steepest in these regions. To highlight the small-scale anomalies of the surface heat flux and quantify their amplitude, we filter out the coefficients of the spherical harmonics of degree l smaller than 30. The filtered profile is plotted according to the right axis of figure 13 in blue. It shows that the heat flux anomalies due to the presence of the zonal flows are sharp and of a small amplitude, approximately 1% of the mean surface heat flux. The thermal signal associated with zonal jets provides useful information in the context of the gas giant planets because the power emitted at the surface of the planet can be measured. For Jupiter and Saturn, the emitted power is approximately uniform in latitude with variations of small amplitude that resemble the structure of the zonal flows at the surface ([Pirraglia, 1984](#); [Li et al., 2010](#)).

For increasing thermal driving (out of reach of our current computational resources), we expect the convective eddies to further enhance the mixing of potential vorticity in the prograde jets. The PV staircase would then become sharper with narrower regions of steep PV gradients, and hence narrower retrograde jets. This sharpening of the PV staircase in rapidly-rotating convection is observed by [Verhoeven & Stellmach \(2014\)](#) at large Rayleigh numbers (20 times supercritical) in 2D numerical simulations using the anelastic approximation. In their study, the β effect is due to the compressibility of the fluid ([Ingersoll & Pollard, 1982](#); [Glatzmaier et al., 2009](#)) and leads to the formation of multiple zonal jets, similarly to the topographic β effect as studied here. They show that the sharpening of the PV staircase results in the sharpening of the entropy staircase (analogous to the temperature staircase in the Boussinesq approximation). In quasi-geostrophic systems with vigorous convection, we thus expect the heat transport process to be heterogeneous with wide convective regions separated by narrow conducting bands; the efficiency of the heat transfer throughout the whole system would largely be controlled by the efficiency of the conducting process across the retrograde jets, and thus, by the width of these conducting bands. This process is partly analogous to the occurrence of layering in double-diffusive convection where the heat transfer is controlled by the flux through the interface between overturning layers ([Turner, 1985](#)).

The main features of the nonlinear quasi-geostrophic dynamics discussed in this paper do not crucially rely on the temperature being 3D. Consequently, we expect that QG models of rotating convection using a 2D temperature field would be able to reproduce our observations qualitatively. QG-2D models could be used to pursue this study at lower Ekman numbers and larger Rayleigh numbers. The numerical framework used in the hybrid QG-3D model is however well suited to explore the possible existence of dynamos driven by quasi-geostrophic flows at low magnetic Prandtl numbers (e.g. [Gillet et al., 2011](#)). The dynamo problem indeed requires to treat the magnetic field in 3D. We shall investigate QG dynamos in a forthcoming study.

Acknowledgements

CG was supported by the Natural Environment Research Council under grant NE/M017893/1. PC acknowledges the Agence Nationale de la Recherche for supporting this project under grant ANR TuDy. This work was undertaken on TOPSY of the HPC facilities at Newcastle University and on the facilities of N8 HPC Centre of Excellence, provided and funded by the N8 consortium and EPSRC (Grant EP/K000225/1) and co-ordinated by the Universities of Leeds and Manchester. We are grateful to the referees for helpful comments that improved the manuscript.

References

- Aubert, J., Brito, D., Nataf, H.-C., Cardin, P., & Masson, J.-P., 2001. A systematic experimental study of rapidly rotating spherical convection in water and liquid gallium, *Phys. Earth and Planet. Int.*, **128**, 51–74.
- Aubert, J., Gillet, N., & Cardin, P., 2003. Quasigeostrophic models of convection in rotating spherical shells, *Geochemistry Geophysics Geosystems*, **4**(7), 1052.
- Aurnou, J., Heimpel, M., Allen, L., King, E., & Wicht, J., 2008. Convective heat transfer and the pattern of thermal emission on the gas giants, *Geophys. J. Int.*, **173**(3), 793–801.
- Aurnou, J. M. & Olson, P. L., 2001. Strong zonal winds from thermal convection in a rotating spherical shell, *Geophys. Res. Lett.*, **28**, 2557–2560.
- Busse, F. H., 1970. Thermal instabilities in rapidly rotating systems, *J. Fluid Mech.*, **44**, 441–460.
- Busse, F. H. & Hood, L. L., 1982. Differential rotation driven by convection in a rapidly rotating annulus, *Geophys. Astrophys. Fluid Dyn.*, **21**(1-2), 59–74.
- Busse, F. H. & Or, A. C., 1986. Convection in a rotating cylindrical annulus: thermal Rossby waves, *J. Fluid Mech.*, **166**, 173–187.
- Cabanes, S., Aurnou, J., Favier, B., & Le Bars, M., 2017. A laboratory model for deep-seated jets on the gas giants, *Nature Physics*, **13**, 387–390.
- Calkins, M., Aurnou, J., Eldredge, J., & Julien, K., 2012. The influence of fluid properties on the morphology of core turbulence and the geomagnetic field, *Earth Planet. Sci. Lett.*, **359**, 55–60.
- Calkins, M. A., Julien, K., & Marti, P., 2013. Three-dimensional quasi-geostrophic convection in the rotating cylindrical annulus with steeply sloping endwalls, *J. Fluid Mech.*, **732**, 214–244.
- Cardin, P. & Olson, P., 1994. Chaotic thermal convection in a rapidly rotating spherical shell: consequences for flow in the outer core, *Phys. Earth Planet. Inter.*, **82**, 235–259.
- Christensen, U. R., 2002. Zonal flow driven by strongly supercritical convection in rotating spherical shells, *J. Fluid Mech.*, **470**, 115–133.
- Davidson, P. A., 2013. *Turbulence in rotating, stratified and electrically conducting fluids*, Cambridge University Press.
- Deguen, R. & Cardin, P., 2009. Tectonic history of the Earth’s inner core preserved in its seismic structure, *Nature Geoscience*, **2**(6), 419–422.

- Dritschel, D. G. & McIntyre, M. E., 2008. Multiple jets as PV staircases: The Phillips effect and the resilience of eddy-transport barriers, *J. Atmos. Sci.*, **65**, 855–874.
- Gastine, T., Heimpel, M., & Wicht, J., 2014. Zonal flow scaling in rapidly-rotating compressible convection, *Phys. Earth Planet. Int.*, **232**, 36–50.
- Gastine, T., Wicht, J., & Aubert, J., 2016. Scaling regimes in spherical shell rotating convection, *J. Fluid Mech.*, **808**, 690–732.
- Gillet, N. & Jones, C. A., 2006. The quasi-geostrophic model for rapidly rotating spherical convection outside the tangent cylinder, *J. Fluid Mech.*, **554**, 343–369.
- Gillet, N., Brito, D., Jault, D., & Nataf, H.-C., 2007. Experimental and numerical study of convection in a rapidly rotating spherical shell, *J. Fluid Mech.*, **580**, 83–121.
- Gillet, N., Schaeffer, N., & Jault, D., 2011. Rationale and geophysical evidence for quasi-geostrophic rapid dynamics within the Earth’s outer core, *Phys. Earth Planet. Inter.*, **187**, 380–390.
- Gilman, P. A., 1977. Nonlinear Dynamics of Boussinesq Convection in a Deep Rotating Spherical Shell. I., *Geophys. Astrophys. Fluid Dyn.*, **8**, 93–135.
- Glatzmaier, G., Evonuk, M., & Rogers, T., 2009. Differential rotation in giant planets maintained by density-stratified turbulent convection, *Geophys. Astrophys. Fluid Dyn.*, **103**, 31–51.
- Goluskin, D., Johnston, H., Flierl, G. R., & Spiegel, E. A., 2014. Convectively driven shear and decreased heat flux, *J. Fluid Mech.*, **759**, 360–385.
- Greenspan, H. P., 1968. *The theory of rotating fluids*, University Press, Cambridge.
- Guervilly, C., 2010. *Dynamos numériques planétaires générées par cisaillement en surface ou chauffage interne*, Ph.D. thesis, Université Joseph Fourier Grenoble, <https://tel.archives-ouvertes.fr/tel-00576177>.
- Guervilly, C. & Cardin, P., 2016. Subcritical convection of liquid metals in a rotating sphere using a quasi-geostrophic model, *J. Fluid Mech.*, **808**, 61–89.
- Guervilly, C., Cardin, P., & Schaeffer, N., 2012. A dynamo driven by zonal jets at the upper surface: Applications to giant planets, *Icarus*, **218**, 100–114.
- Heimpel, M. & Aurnou, J., 2007. Turbulent convection in rapidly rotating spherical shells: A model for equatorial and high latitude jets on Jupiter and Saturn, *Icarus*, **187**(2), 540–557.
- Heimpel, M., Aurnou, J., & Wicht, J., 2005. Simulation of equatorial and high-latitude jets on Jupiter in a deep convection model, *Nature*, **438**, 193–196.
- Ingersoll, A. P. & Pollard, D., 1982. Motion in the interiors and atmospheres of Jupiter and Saturn - Scale analysis, anelastic equations, barotropic stability criterion, *Icarus*, **52**, 62–80.
- Jones, C. A., 2015. Thermal and compositional convection in the outer core, in *Treatise on Geophysics*, pp. 115 – 159, ed. Schubert, G., Elsevier, Oxford, second edition edn.
- Jones, C. A., Soward, A. M., & Mussa, A. I., 2000. The onset of thermal convection in a rapidly rotating sphere, *J. Fluid Mech.*, **405**, 157–179.
- Jones, C. A., Rotvig, J., & Abdulrahman, A., 2003. Multiple jets and zonal flow on Jupiter, *Geophys. Res. Lett.*, **30**(14), 140000.
- Kaplan, E. J., Schaeffer, N., Vidal, J., & Cardin, P., 2017. Subcritical thermal convection of liquid metals in a rotating sphere, *accepted in Phys. Rev. Lett.*
- Kuo, H.-L., 1949. Dynamic instability of two-dimensional nondivergent flow in a barotropic atmosphere., *J. Atmos. Sci.*, **6**, 105–122.
- Labbé, F., Jault, D., & Gillet, N., 2015. On magnetostrophic inertia-less waves in quasi-geostrophic models of planetary cores, *Geophys. Astrophys. Fluid Dyn.*, **109**(6), 587–610.

- Li, L., Conrath, B. J., Gierasch, P. J., Achterberg, R. K., Nixon, C. A., Simon-Miller, A. A., Flasar, F. M., Banfield, D., Baines, K. H., West, R. A., & et al., 2010. Saturn’s emitted power, *J. Geophys. Res.*, **115**(E11).
- Livermore, P. W., Hollerbach, R., & Finlay, C. C., 2017. An accelerating high-latitude jet in Earth’s core, *Nature Geoscience*, **10**(1), 62–68.
- McIntyre, M. E., 2003. Potential vorticity, *Encyclopedia of Atmospheric Sciences*, **2**, 685–694.
- McIntyre, M. E., 2008. Potential-vorticity inversion and the wave-turbulence jigsaw: some recent clarifications, *Adv. Geosci.*, **15**, 47–56.
- Miyagoshi, T., Kageyama, A., & Sato, T., 2010. Zonal flow formation in the Earth’s core, *Nature*, **463**, 793–796.
- Morin, V. & Dormy, E., 2004. Time dependent beta-convection in rapidly rotating spherical shells, *Phys. Fluids*, **16**(5), 1603–1609.
- Or, A. C. & Busse, F. H., 1987. Convection in a rotating cylindrical annulus. II. Transitions to asymmetric and vacillating flow., *J. Fluid Mech.*, **174**, 313–326.
- Pedlosky, J., 1987. *Geophysical fluid dynamics*, Springer, New York.
- Pirraglia, J. A., 1984. Meridional energy balance of jupiter, *Icarus*, **59**(2), 169–176.
- Plaut, E., Lebranchu, Y., Simatev, R., & Busse, F. H., 2008. On the Reynolds stresses and mean fields generated by pure waves: Applications to shear flows and convection in a rotating shell, *J. Fluid Mech.*, **602**, 303–326.
- Porco, C. C., West, R. A., McEwen, A., Del Genio, A. D., Ingersoll, A. P., Thomas, P., Squyres, S., Dones, L., Murray, C. D., Johnson, T. V., Burns, J. A., Brahic, A., Neukum, G., Veverka, J., Barbara, J. M., Denk, T., Evans, M., Ferrier, J. J., Geissler, P., Helfenstein, P., Roatsch, T., Throop, H., Tiscareno, M., & Vasavada, A. R., 2003. Cassini imaging of Jupiter’s atmosphere, satellites, and rings, *Science*, **299**, 1541–1547.
- Read, P. L., Jacoby, T. N. L., Rogberg, P. H. T., Wordsworth, R. D., Yamazaki, Y. H., Miki-Yamazaki, K., Young, R. M. B., Sommeria, J., Didelle, H., & Viboud, S., 2015. An experimental study of multiple zonal jet formation in rotating, thermally driven convective flows on a topographic beta-plane, *Phys. Fluids*, **27**(8), 085111.
- Rhines, P., 1975. Waves and turbulence on a beta-plane, *J. Fluid Mech.*, **69**, 417–443.
- Rotvig, J., 2007. Multiple zonal jets and drifting: Thermal convection in a rapidly rotating spherical shell compared to a quasigeostrophic model, *Phys. Rev. E*, **76**(4), 046306.
- Schaeffer, N. & Cardin, P., 2005. Quasigeostrophic model of the instabilities of the Stewartson layer in flat and depth-varying containers, *Phys. Fluids*, **17**(10), 104111.
- Schou, J., Antia, H. M., Basu, S., Bogart, R. S., Bush, R. I., Chitre, S. M., Christensen-Dalsgaard, J., Di Mauro, M. P., Dziembowski, W. A., Eff-Darwich, A., & Gough, D. O., 1998. Helioseismic studies of differential rotation in the solar envelope by the solar oscillations investigation using the Michelson Doppler Imager, *Astrophys. J.*, **505**(1), 390–417.
- Scott, R. K. & Dritschel, D. G., 2012. The structure of zonal jets in geostrophic turbulence, *J. Fluid Mech.*, **711**, 576–598.
- Smith, C. A., Speer, K. G., & Griffiths, R. W., 2014. Multiple zonal jets in a differentially heated rotating annulus, *J. Phys. Ocean.*, **44**(9), 2273–2291.
- Soward, A. M., 1977. On the finite amplitude thermal instability of a rapidly rotating fluid sphere, *Geophys. Astrophys. Fluid Dyn.*, **9**(1), 19–74.
- Sukoriansky, S., Dikovskaya, N., & Galperin, B., 2007. On the arrest of inverse energy cascade and the Rhines scale, *J. Atmos. Sci.*, **64**, 3312.

- Sumita, I. & Olson, P., 2000. Laboratory experiments on high Rayleigh number thermal convection in a rapidly rotating hemispherical shell, *Phys. Earth Planet. Int.*, **117**, 153–170.
- Teed, R., Jones, C., & Hollerbach, R., 2012. On the necessary conditions for bursts of convection within the rapidly rotating cylindrical annulus, *Phys. Fluids*, **24**(6), 066604.
- Turner, J. S., 1985. Multicomponent convection, *Annu. Rev. Fluid Mech.*, **17**(1), 11–44.
- Vallis, G. K., 2006. *Atmospheric and oceanic fluid dynamics: fundamentals and large-scale circulation*, Cambridge University Press.
- Verhoeven, J. & Stellmach, S., 2014. The compressional beta effect: A source of zonal winds in planets?, *Icarus*, **237**, 143–158.
- von Hardenberg, J., Goluskin, D., Provenzale, A., & Spiegel, E. A., 2015. Generation of large-scale winds in horizontally anisotropic convection, *Phys. Rev. Lett.*, **115**(13), 134501.
- Yadav, R., Gastine, T., Christensen, U., Duarte, L., & Reiners, A., 2016. Effect of shear and magnetic field on the heat-transfer efficiency of convection in rotating spherical shells, *Geophys. J. Int.*, **204**(2), 1120–1133.
- Yoshida, S., Sumita, I., & Kumazawa, M., 1996. Growth model of the inner core coupled with the outer core dynamics and the resulting elastic anisotropy, *J. Geophys. Res.*, **101**, 28085–28104.
- Zhang, K., 1991. Convection in a rapidly rotating spherical shell at infinite Prandtl number: steadily drifting rolls, *Phys. Earth Planet. Int.*, **68**(1-2), 156–169.
- Zhang, K., 1992. Spiralling columnar convection in rapidly rotating spherical fluid shells, *J. Fluid Mech.*, **236**, 535–556.